

Journal Pre-proofs

Lanthanide complexes with *N*-(2,6-dimethylphenyl)oxamate: Synthesis, characterisation and cytotoxicity

Tatenda Madanhire, Hajierah Davids, Melanie C. Pereira, Eric C. Hosten, Abubak'r Abrahams

PII: S0277-5387(20)30218-7
DOI: <https://doi.org/10.1016/j.poly.2020.114561>
Reference: POLY 114561

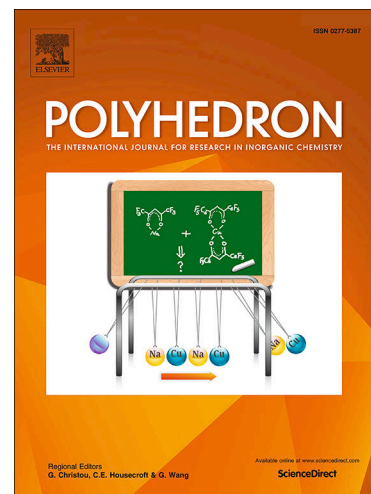
To appear in: *Polyhedron*

Received Date: 9 March 2020
Revised Date: 26 March 2020
Accepted Date: 28 March 2020

Please cite this article as: T. Madanhire, H. Davids, M.C. Pereira, E.C. Hosten, A. Abrahams, Lanthanide complexes with *N*-(2,6-dimethylphenyl)oxamate: Synthesis, characterisation and cytotoxicity, *Polyhedron* (2020), doi: <https://doi.org/10.1016/j.poly.2020.114561>

This is a PDF file of an article that has undergone enhancements after acceptance, such as the addition of a cover page and metadata, and formatting for readability, but it is not yet the definitive version of record. This version will undergo additional copyediting, typesetting and review before it is published in its final form, but we are providing this version to give early visibility of the article. Please note that, during the production process, errors may be discovered which could affect the content, and all legal disclaimers that apply to the journal pertain.

© 2020 Published by Elsevier Ltd.



Lanthanide complexes with *N*-(2,6-dimethylphenyl)oxamate: Synthesis, characterisation and cytotoxicity

Tatenda Madanhire, Hajierah Davids, Melanie C. Pereira, Eric C. Hosten and Abubak'r Abrahams*

Email: Abubakr.Abrahams@mandela.ac.za

*School of Biomolecular and Chemical Sciences, PO Box 77000, Nelson Mandela University,
Port Elizabeth, 6031, South Africa*

ABSTRACT

The complexation reactions of Ce(III), Nd(III), Gd(III) and Er(III) ions with the chelating/bridging monoanionic ligand *N*-(2,6-dimethylphenyl)oxamate (Hpma⁻) in basic media were performed in view of the potential applications of oxamate derivatives as cytotoxic agents. The coordination compounds were characterised by different physico-chemical techniques: elemental analysis, conductivity measurements, IR, ¹H NMR and UV-Vis-NIR spectroscopy, and X-ray crystallography. The anionic Hpma⁻ ligand was obtained through conversion of the proligand ethyl (2,6-dimethylphenylcarbamoyl)formate (Hdmp). The reactions afforded lanthanide(III)-oxamate coordination polymers of the formulae: {[Ln(Hpma)₃(MeOH)(H₂O)]·2MeOH}_n (Ln = Ce (1) and Nd (2)), {[Gd₂(Hpma)₆(MeOH)₄]·6MeOH}_n (3), {[Er₂(Hpma)₆(MeOH)(H₂O)₃]·2MeOH}_n (4) and [Ln₂Na₂(Hpma)₈(EtOH)(H₂O)₆]_n (Ln = Nd (5) and Gd (6)). The polymeric complexes feature Ln-Hpma moieties bridged by μ₂-η¹:η¹:η¹ Hpma⁻ ligands, giving one-dimensional zig-zag chains of the -Ln-O-C-O-Ln- type. Atomic charge analysis and the MEP map of the Hpma⁻ moiety using the DFT/B3LYP method were consistent with the chelating and bridging modes of the anionic ligand through all the oxygen atoms. An evaluation of the cytotoxic activities of the metal salts, the proligand and the novel lanthanide complexes on MCF-7, HEC-1A and THP-1 cells revealed that only the rare-earth metal salts [Ce(NO₃)₃·6H₂O] and [Nd(NO₃)₃·6H₂O] showed moderate cytotoxicity against MCF-7 and HEC-1A cells, respectively.

Keywords: Complexes, oxamate, bidentate, bridging, heterometallic, natural charge, cytotoxicity

1. Introduction

The prevalence of cancer is rising each year, resulting in cancer becoming the leading cause of death worldwide [1]. Among the most commonly diagnosed types of cancers are breast (in women), endometrial, prostate, colorectal and lung cancer [1-4]. The metallodrug cisplatin has been extensively used in cancer chemotherapy since the 1960s, although its clinical applications are limited due to adverse effects, such as nausea, ototoxicity, low hydrolytic stability and resistance in some cancer cells [5,6]. This has encouraged researchers to investigate alternative metal complexes as potential anticancer agents with improved effectiveness towards cancer.

Previous studies have demonstrated that complexes of the *4f* elements have a relevant role in chemotherapy, since Ln(III) compounds actively inhibit tumour growth due to the ability of the lanthanide ion to suppress iron uptake, alter signal transduction and inhibit reactive oxygen species production through binding to hydro-peroxides [7,8]. In addition, lanthanides can mask free radicals by means of magnetic interactions [7]. Limitations associated with platinum-based anticancer agents can thus potentially be overcome by resorting to lanthanide-based drugs.

The *d*- and *f*-block metal complexes containing carboxylic acids have been widely studied due to their potential use as anticancer agents [9]. Oxamic acid is amongst the simplest carboxylic acid ligands examined (Figure 1), which has tumour growth inhibition properties [9-11]. Oxamate (a structural analogue of pyruvate), or its derivatives, act by targeting aerobic glycolysis (an abnormal process related to tumour progression and metastasis) through the competitive inhibition of pyruvate conversion to lactate by lactate dehydrogenase A (LDHA) [9-11]. For example, oxamate significantly inhibits the proliferation of non-small cell lung cancer (NSCLC) cells, with the investigation revealing lower toxicity in normal cells [12].

Complexation studies of oxamic acid and its derivatives with *d*- and *f*-block metals indicated that these ligands have interesting ligating properties, as they chelate in a bidentate mode to the metal ions, either *via* both oxygen atoms, or through one nitrogen atom and one oxygen atom [9,13]. For example, X-ray analysis of the Co(III) complex $[\text{Co}(\text{C}_2\text{O}_3\text{NH}_2)_2(\text{OH}_2)_2] \cdot 2\text{H}_2\text{O}$ revealed coordination of oxamic acid as a bidentate *O,O*-donor

ligand. Other reports showed that oxamic acid can act mono-, bi-, tri- or tetradentately (bridging) in its mono- or dianionic form [9,13]. Monodentate coordination is possible for the monoanionic ligand using an *O*-atom of the carboxylic group, while tridentate binding occurs through all the oxygen atoms. The carboxylic and amide protons are ionisable to yield a dianionic ligand, which can act as a bridging ligand in dinuclear or polynuclear complexes [13].

Lanthanide complexes are vital, not only in chemotherapy, but also in cancer diagnosis, due to the versatile magnetic characteristics of the metal ion $4f$ electronic configuration [14]. An example of a complex showing slow magnetic relaxation behaviour is the mononuclear Dy(III)-oxamate complex derived from *N*-(2,6-dimethylphenyl)oxamic acid (H_2L , Figure 1) in a controlled basic media [15]. The isolated mononuclear Dy(III) coordination compound, which is stabilised by metal-ligand bonds and hydrogen bonding, has the formula $Me_4N[Dy(HL)_4] \cdot 2CH_3CN$. The oxamate ligands assume the *O,O'*-chelating mode, forming an eight-coordinate environment with a distorted D_{2d} dodecahedron geometry [15].

This paper reports on the preparation of the solid-state Ce(III), Nd(III), Gd(III) and Er(III) complexes with *N*-(2,6-dimethylphenyl)oxamate ($Hpma^-$) (Scheme 1) and their characterisation by means of micro-analyses, infrared (IR), ultraviolet-visible-near infrared (UV-Vis-NIR) and nuclear magnetic resonance (NMR) spectroscopy, as well as single-crystal X-ray crystallography. We herein present Ln(III)-oxamate coordination polymers of the formula: $\{[Ln(Hpma)_3(MeOH)(H_2O)] \cdot 2MeOH\}_n$ ($Ln = Ce$ (1) and Nd (2)), $\{[Gd_2(Hpma)_6(MeOH)_4] \cdot 6MeOH\}_n$ (3), $\{[Er_2(Hpma)_6(MeOH)(H_2O)_3] \cdot 2MeOH\}_n$ (4) and $[Ln_2Na_2(Hpma)_8(EtOH)(H_2O)_6]_n$ ($Ln = Nd$ (5) and Gd (6)). Density Functional Theory (DFT) calculations were performed to compare theoretical calculations and experimental findings, and to confirm the experimental results. This work also aims at screening the anticancer effects of the oxamate compounds by determining their *in vitro* cytotoxicities against breast cancer (MCF-7), endometrial carcinoma (HEC-1A) and human monocytic (THP-1) cell lines, using a 3-(4,5-dimethylthiazol-2-yl)-2,5-diphenyltetrazolium bromide (MTT) assay [16,17]. The anticancer studies serve to identify compounds that may act as lead compounds in the design of novel chemotherapeutic agents.

2. Experimental

2.1. General procedures

All chemicals and reagents were of analytical grade and were used without further purification. The melting points and CHN analyses of compounds were performed on a Stuart® Melting Point Apparatus SMP30 and an Elementar Vario EL Cube Elemental Analyzer, respectively. A HANNA instruments (HI) 2300 EC/TDS/NaCl Meter was used for the conductivity measurements. Nuclear Magnetic Resonance spectra were obtained at room temperature using a Bruker AvanceIII 400 NMR spectrometer and analysis of the spectra was performed using *ACD/Labs* software (version 12.0, 1997–2008). The infrared spectra were recorded on a Bruker Tensor 27 FT-IR spectrophotometer, equipped with the platinum attenuated total reflection (ATR) attachment. The samples were run neat on ATR and the recorded data were analysed using the *OPUS 6.5* software. Signal intensities were denoted by the following abbreviations: w = weak, m = medium, s = strong and b = broad. The UV-Vis spectra of the compounds were investigated using a PerkinElmer Lambda 35 UV/Vis spectrophotometer and processing was completed using *UV WinLab* software (v1.0.0). Single crystal X-ray diffraction on crystals of Hdmp and **1–6** was performed using a Bruker Kappa Apex II X-ray Crystallography System at 296 K (Hdmp) and 200 K (**1–6**), using graphite monochromated Mo K α radiation ($\lambda = 0.71073 \text{ \AA}$). Molecular graphics were obtained using *ORTEP* for Windows v2014.1 and *Mercury 3.6* software [18,19]. Lanthanide geometry analyses, through calculation of continuous shape measures (CShM values) were enabled by the *SHAPE 2.1* software, while the polyhedral views were generated using *VESTA* software (version 3, 2006–2014) [20,21].

2.2. X-ray crystallographic measurements

A summary of the crystal data, data collection and refinement parameters for the proligand and complexes **1–6** is presented in Table 1. APEX2 (ver. 2014.11-0) was used for data collection and the data were integrated via SAINT software (ver. 8.34A) [22]. The structures were solved by direct methods utilising SHELXT-2018/2 and refined by least-squares procedures using SHELXL-2018/3 with ShelXle as a graphical interface [23–25]. Empirical absorption corrections were performed using the numerical method implemented in SADABS [22]. All non-hydrogen atoms were refined anisotropically, while carbon-bound *H*-atoms

were placed in calculated positions and refined isotropically in the riding model approximation, with $U_{\text{iso}}(\text{H})$ set to $1.2U_{\text{eq}}(\text{C})$. The H -atoms of the methyl groups were permitted to rotate with a fixed angle around the C—C bond to best fit the experimental electron density (HFIX 137 in the SHELX program suite), with $U_{\text{iso}}(\text{H})$ set to $1.5U_{\text{eq}}(\text{C})$ [24]. The hydroxyl group H -atoms were rotated with a fixed angle around the C—O bond to best fit the experimental electron density (HFIX 147 in the SHELX program suite), with $U_{\text{iso}}(\text{H})$ set to $1.5U_{\text{eq}}(\text{O})$ [24]. The nitrogen-bound H -atoms were located on a difference Fourier map and refined freely.

2.3. Molecular modelling

Molecular geometries of Hpma^- in DMSO and the gaseous phase were optimised using Density Functional Theory (DFT) calculations, employing the Becke3-Lee-Yang-Parr (B3LYP) model and aug-cc-pVTZ basis set [26,27]. The calculations were performed using the *Gaussian 16* program package (Rev. B01). After optimisation, single-point energy calculations were performed, upon which natural bond orbital (NBO) analysis was done using the *NBO 6.0* program [NBO 6.0.19 (05-Aug-2018)] [28-30]. Natural Population Analysis (NPA) was used to determine the atomic charges of the monoanionic ligand in solution and in the gaseous phase [31]. The surface molecular electrostatic potential (MEP) values were computed and the electron density distribution, molecular shape and size in three-dimensions were visualised employing *MoleCoolQt64* software (2003–2012) [32]. The *Avogadro* software (version 2, 1991) was used in visualising the highest occupied molecular orbitals (*HOMO*) and lowest unoccupied molecular orbitals (*LUMO*).

2.4. Procedures for *in vitro* anticancer analyses

2.4.1. Cell culture and maintenance

The MCF-7 and HEC-1A cancer cells were routinely maintained in 25 or 75 cm² cell culture flasks as monolayer cultures, in growth medium consisting of DMEM supplemented with 10% heat-inactivated foetal bovine serum (HI-FBS), while the THP-1 cells were regularly maintained in RPMI-1640 medium supplemented with 10% HI-FBS. The cells were maintained at 37 °C in a humidified atmosphere (5% CO₂ and 95% air).

2.4.2. Preparation of the compounds and controls

100 mM stock solutions of the test agents were prepared in DMSO (100%) and diluted to give final well concentrations of DMSO less than 0.1%, which did not adversely affect cell growth. The 0.1% DMSO was used as a vehicle control. Dilutions with complete growth medium were obtained from stock solutions, to give final well concentrations of 100 μ M. A biologically active component of the Indian *Curcuma longa* plant (turmeric), curcumin, was used as a positive control [33,34]. The anticancer properties of curcumin against multiple human carcinomas, including breast, ovarian, prostate, colon, pancreatic, and head and neck cancers, are ascribed to its ability to target multiple pathways that effect cellular death. The mechanisms of action of the compound include its effect in biological pathways or on various growth factor receptors associated with cell cycle regulation, apoptosis, mutagenesis, metastasis, oncogene expression, angiogenesis and tumorigenesis [33,34].

2.4.3. Cell counting using Trypan blue

The Trypan blue exclusion assay is an important method in cell viability determination [35,36]. This test depends on the ability of non-viable cells (plasma membrane integrity lost) to incorporate Trypan blue, while viable cells (intact plasma membranes) exclude the stain. Under light microscopy, non-viable cells appear dark blue, whilst viable cells appear colourless [35,36]. Cell counting was performed utilising a Neubauer counting chamber (Superior). Staining of the cells was done with Trypan blue (4%) in a ratio of 1:1. The total number of cells/mL was calculated as: the average cell count per square \times dilution factor \times 10^4 .

2.4.4. Cell viability determination using an MTT assay

The cytotoxic activity of the investigated compounds was assessed by a 3-(4,5-dimethylthiazol-2-yl)-2,5-diphenyltetrazolium bromide (MTT) assay, which relies on the cellular metabolic activity of NAD(P)H-dependent oxidoreductase enzymes [16,17,37]. This dye reduction assay is based on the reduction of the pale yellow tetrazolium salt (MTT) to purple formazan crystals in viable cells [16,17].

The cells were seeded in 96-well tissue culture plates at a density of 10^4 cells/well in complete growth medium. After an overnight incubation (37 $^{\circ}$ C), the cells were treated with

the test compounds and the controls for 24 hours, at a final well concentration of 100 μ M. Subsequently, MTT (0.5 mg/mL, 100 μ L) was added to each well. For the suspension (THP-1) cells, MTT (2.5 mg/mL) was added to the cells at 20 % v/v. The plates were then incubated for 3 hours at 37 °C, and the purple formazan crystals that formed were solubilised in 100 μ L DMSO (100%). Absorbance values were read against a DMSO blank, at 540 nm, using a ThermoMultiSkan Go microplate reader (Thermo Scientific, U.S.A.). Background interference in THP-1 cell suspensions was corrected by setting up sample background controls using equal volumes of cell culture media and MTT reagent.

The number of viable cells was extrapolated from an MTT standard curve per cell line and the percentage cell viability was determined as a percentage of the 0.1% DMSO vehicle control. Each experiment was completed in triplicate.

2.4.5. Statistical analysis

All data are reported as mean \pm S.D. for triplicate experiments ($n = 3$). ANOVA was used in the analysis of non-parametric grouping of data, whilst secondary data analysis for significance was performed with Student's t-test. Values of $p < 0.05$ were regarded significant.

2.5. Synthesis of ethyl (2,6-dimethylphenylcarbamoyl)formate (Hdmp)

The proligand Hdmp was synthesised according to the literature procedure [38]. 2,6-Dimethylphenylaniline (10.22 mL, 83 mmol) in 250 mL THF was treated with 9.3 mL ethyl chlorooxoacetate (9.273 mL, 83 mmol) in the presence of 12 mL triethyl amine (11.569 mL, 83.002 mmol). The mixture was continuously stirred for 30 minutes at room temperature, under a nitrogen atmosphere. The resulting solution was filtered and the solvent was removed under vacuum to yield an oily, colourless crude product, which quickly solidified. The white solid was suspended in water and filtered off, washed with diethyl ether and then dried under vacuum. Yield: 93.0%, m.p.: 177.1 °C. Anal. *Calcd* for $C_{12}H_{15}NO_3$ (%): C, 65.14; H, 6.83; N, 6.33. Found: C, 65.12; H, 6.78; N, 6.27. IR (cm^{-1}): $\nu(N-H)$ 3252(s); $\nu(C-H)$ 3060, 2980, 2936(w); $\nu(C=O)$ 1763, 1688(s); $\nu(C=C)$ 1525(s); $\nu(C-O-C)$ 1298–1176(m). 1H NMR (400 MHz, $DMSO-d_6$, δ ppm): 1.33 (t, $J = 6.97$ Hz, 3H), 2.14 (s, 6H), 4.31 (q, $J = 7.17$ Hz, 2H),

7.11 (m, 3H), 10.29 (br s, 1H). ^{13}C NMR (400 MHz, DMSO- d_6 , δ ppm): 14.34, 18.36, 62.73, 127.64, 128.27, 134.09, 135.59, 156.25, 161.32.

2.6. Synthesis of complexes 1–4

A mixture of 3 mL 1M NaOH and Hdmp (≈ 3 mmol) was heated until the ligand dissolved. An aqueous solution of 1 mmol $[\text{Ln}(\text{NO}_3)_3 \cdot x\text{H}_2\text{O}]$ (Ln = Ce, Nd, Gd and Er) was mixed with the ligand solution. The resulting white precipitate was filtered, washed with distilled water and diethyl ether, and then dried. Dissolution in methanol, followed by slow diffusion of diethyl ether into the solution resulted in X-ray quality crystals within 5 days (Scheme 2).

2.6.1. $\{[\text{Ce}(\text{Hpma})_3(\text{MeOH})(\text{H}_2\text{O})] \cdot 2\text{MeOH}\}_n$ (1)

Hdmp (0.664 g, 3 mmol), 1 M NaOH (3 mL), $[\text{Ce}(\text{NO}_3)_3 \cdot 6\text{H}_2\text{O}]$ (0.434 g, 1 mmol). Yield: 0.536 g (64.5% based on the Ce(III) salt); white crystals, m.p.: > 300.0 °C. Anal. *Calcd.* for $\text{C}_{31}\text{H}_{36}\text{CeN}_3\text{O}_{11} \cdot 2(\text{CH}_4\text{O})$ (%): C, 47.71; H, 5.34; N, 5.06. Found: C, 47.63; H, 5.19; N, 5.26. Conductivity (10^{-3} M, DMF, $\text{ohm}^{-1} \text{cm}^2 \text{mol}^{-1}$): 3.55. IR (cm^{-1}): $\nu(\text{O-H})$ 3613–3125(b); $\nu(\text{C-H})$ 3052–2931(w); $\nu(\text{C=O})$ 1635(s); $\nu(\text{Ln-O})$ 447(w).

2.6.2. $\{[\text{Nd}(\text{Hpma})_3(\text{MeOH})(\text{H}_2\text{O})] \cdot 2\text{MeOH}\}_n$ (2)

Hdmp (0.662 g, 2.992 mmol), 1 M NaOH (3 mL), $[\text{Nd}(\text{NO}_3)_3 \cdot 6\text{H}_2\text{O}]$ (0.437 g, 0.997 mmol). Yield: 0.531 g (63.7% based on the Nd(III) salt); purple crystals, m.p.: > 300.0 °C. Anal. *Calcd.* for $\text{C}_{31}\text{H}_{35}\text{NdN}_3\text{O}_{11} \cdot 2(\text{CH}_4\text{O})$ (%): C, 47.53; H, 5.20; N, 5.04. Found: C, 47.45; H, 5.18; N, 5.07. Conductivity (10^{-3} M, DMF, $\text{ohm}^{-1} \text{cm}^2 \text{mol}^{-1}$): 3.58. IR (cm^{-1}): $\nu(\text{O-H})$ 3613–3125(b); $\nu(\text{C-H})$ 3052–2931(w); $\nu(\text{C=O})$ 1635(s); $\nu(\text{Ln-O})$ 450(w).

2.6.3. $\{[\text{Gd}_2(\text{Hpma})_6(\text{MeOH})_4] \cdot 6\text{MeOH}\}_n$ (3)

Hdmp (0.663 g, 2.996 mmol), 1 M NaOH (3 mL), $[\text{Gd}(\text{NO}_3)_3 \cdot 6\text{H}_2\text{O}]$ (0.452 g, 1.001 mmol). Yield: 0.497 g (55.6% based on the Gd(III) salt); white crystals, m.p.: > 300.0 °C. Anal. *Calcd.* for $\text{C}_{64}\text{H}_{76}\text{Gd}_2\text{N}_6\text{O}_{22} \cdot 6(\text{CH}_4\text{O})$ (%): C, 47.02; H, 5.64; N, 4.70. Found: C, 47.12; H, 5.48; N, 4.82. Conductivity (10^{-3} M, DMF, $\text{ohm}^{-1} \text{cm}^2 \text{mol}^{-1}$): 14.45. IR (cm^{-1}): $\nu(\text{O-H})$ 3613–3125(b); $\nu(\text{C-H})$ 3052–2929(w); $\nu(\text{C=O})$ 1635(s); $\nu(\text{Ln-O})$ 447(w).

2.6.4. $\{[\text{Er}_2(\text{Hpma})_6(\text{MeOH})(\text{H}_2\text{O})_3] \cdot 2\text{MeOH}\}_n$ (4)

Hdmp (0.664 g, 3 mmol), 1 M NaOH (3 mL), [Er(NO₃)₃·5H₂O] (0.443 g, 0.999 mmol). Yield: 0.578 g (70.6% based on the Ce(III) salt); pink crystals, m.p.: 278.3 °C. Anal. *Calcd.* for C₆₁H₇₀Er₂N₆O₂₂, 2(CH₄O) (%): C, 46.20; H, 4.80; N, 5.13. Found: C, 46.48; H, 4.74; N, 5.33. Conductivity (10⁻³ M, DMF, ohm⁻¹ cm² mol⁻¹): 51.90. IR (cm⁻¹): ν(O-H) 3613–3125(b); ν(C-H) 3052–2929(w); ν(C=O) 1637(s); ν(Ln-O) 447(w).

2.7. Synthesis of complexes 5 and 6

A mixture of 3 mmol Hdmp dispersed in water and 3 mL 1M NaOH was heated until the ligand dissolved. A 1 mmol [Ln(NO₃)₃·6H₂O] (Ln = Nd and Gd) aqueous solution was added to the ligand solution, and a white precipitate formed. The mixture was refluxed, and then methanol was added until the precipitate dissolved. The solution was cooled and kept at room temperature until single crystals formed after 7 days.

2.7.1. [Nd₂Na₂(Hpma)₈(EtOH)(H₂O)₆]_n (5)

Hdmp (0.666 g, 3.010 mmol), 1 M NaOH (3 mL), [Nd(NO₃)₃·6H₂O] (0.438 g, 1 mmol). Yield: 0.489 g (48.3% based on the Nd(III) salt); purple crystals, m.p.: 276.8 °C. Anal. *Calcd.* for C₈₂H_{95.54}N₈Na₂Nd₂O_{30.46}, C₂H₆O, O (%): C, 48.58; H, 4.93; N, 5.40. Found: C, 48.51; H, 4.68; N, 5.79. Conductivity (10⁻³ M, DMF, ohm⁻¹ cm² mol⁻¹): 46.90. IR (cm⁻¹): ν(O-H) 3613–3125(b); ν(C-H) 3052–2929(w); ν(C=O) 1635(s); ν(Ln-O) 452(w).

2.7.2. [Gd₂Na₂(Hpma)₈(EtOH)(H₂O)₆]_n (6)

Hdmp (0.660 g, 2.978 mmol), 1 M NaOH (3 mL), [Gd(NO₃)₃·6H₂O] (0.453 g, 1 mmol). Yield: 0.493 g (48.2% based on the Ce(III) salt); white crystals, m.p.: 277.5 °C. Anal. *Calcd.* for C_{81.41}H_{94.22}Gd₂N₈Na₂O_{30.30}, C₂H₆O, O (%): C, 47.89; H, 4.83; N, 5.36. Found: C, 47.84; H, 4.67; N, 5.35. Conductivity (10⁻³ M, DMF, ohm⁻¹ cm² mol⁻¹): 53.40. IR (cm⁻¹): ν(O-H) 3613–3125(b); ν(C-H) 3052–2929(w); ν(C=O) 1636(s); ν(Ln-O) 447(w).

3. Results and discussion

3.1. Synthesis, FT-IR and NMR spectroscopy

The use of basic media in the preparation of the coordination compounds resulted in the conversion of the proligand Hdmp to the anionic Hpma⁻ [38].

The infrared spectra of the proligand Hdmp and its Ln(III) complexes (Figure 2) exhibit similar spectral features due to their related coordination environments [39]. The strong $\nu(\text{N-H})$ band of Hdmp located at 3252 cm^{-1} is replaced by broad bands in **1–6** in the region $3613\text{--}3125\text{ cm}^{-1}$, indicating the presence of O-H stretching vibrations of water or methanol molecules in the metal complexes [38,40,41]. The high frequency spectral region of the proligand Hdmp also exhibits typical C-H vibrations (3060 , 2980 and 2936 cm^{-1}), while the C-H vibrations of the phenyl rings of the oxamate ligands in the complexes show a slight red-shift ($3052\text{--}2929\text{ cm}^{-1}$) relative to Hdmp [38]. Two strong absorptions occurring at 1763 and 1688 cm^{-1} correspond to the characteristic C=O stretching vibrations in Hdmp [38,42]. These strong $\nu(\text{C=O})$ appear as single bands in all the title complexes, at approximately 1635 cm^{-1} , hence confirming the role of the oxamate oxygen atoms in coordination [38,42]. A series of four absorption peaks in the range $1298\text{--}1176\text{ cm}^{-1}$, typical of C-O-C bonds, are observed for the free ligand. The latter disappear upon coordination, thus confirming the complete conversion of Hdmp to Hpma⁻ [40]. After complexation, weak Ln-O vibrations are assigned to the bands found at $452\text{--}447\text{ cm}^{-1}$, which show the involvement of the oxygen atoms in the primary coordination sphere of the lanthanide(III) ions [40,43].

Nuclear magnetic resonance experiments on Hdmp and the complexes were performed in DMSO-*d*₆ (Figure 3). For complexes **3**, **4** and **6**, the paramagnetic nature of the Gd(III) and Er(III) ions gave rise to signal broadening and featureless ¹H NMR spectra, while complexes **1**, **2** and **5** gave clearly defined spectra, though there appears discernible evidence of some broadening [44]. In concurrence with the IR spectral and X-ray crystallographic data, the ¹H-NMR spectra of the coordination compounds **1**, **2** and **5** clearly show formation of the Hpma⁻ anion from Hdmp, as indicated by the disappearance of the ethyl group signals after coordination [38]. The N-H group peaks of the ligand gives a broad signal in **1** (δ 12.29 ppm), but similar peaks are not seen in the spectra of **2** and **5**, suggesting participation of the oxamate moieties in ligand coordination [38]. The spectra of the complexes also exhibit Hpma⁻ methyl proton signals, peaking at δ 1.55, 1.57 and 1.51 ppm, an indication that the methyl groups undergo a significant shift in the chemical environment relative to Hdmp (δ 2.14 ppm) upon hydrolysis [45]. Downfield to the methyl proton peaks of **1**, **2** and **5**, are resonances attributable to the aromatic proton signals of the oxamate ligands (δ 6.37–6.57 ppm), which are also more shielded than the proligand aromatic protons (δ 7.11 ppm).

3.2. UV-Vis-NIR spectroscopy

The ligand Hdmp and the trivalent complexes of Ce(III) and Gd(III) (complexes **1** and **3**) have no significant absorption in the ultraviolet, visible and near-infrared regions. The UV-Vis-NIR spectra of **2**, **4**, **5** and **6** are displayed in Figure 4 and the assignment of absorption bands is shown in Table 2. Absorption peaks of the Nd(III), Er(III) and Gd(III) complexes arise from the Laporte-forbidden $f-f$ transitions from the ground level of $^4I_{9/2}$, $^4I_{15/2}$ and $^8S_{7/2}$, respectively, to the excited J -levels of the $4f$ -configuration [46-51]. The spectra of **2** and **5** are similar, with absorption maxima at 511, 522, 582 and 745 nm in the visible region, corresponding to transitions from the $^4I_{9/2}$ ground level to the excited J -levels $^4G_{9/2}$, $^4G_{7/2}$, $^4G_{5/2} + ^2G_{7/2}$ and $^4F_{7/2} + ^4S_{3/2}$, respectively [46-48,51,52]. The peak observed in the NIR region at 800 nm is assigned to the $f-f$ transition from the ground level to the $4f$ -configurations $^4F_{5/2} + ^2H_{9/2}$, while those appearing at 869 and 876 nm are attributed to a transition from $^4I_{9/2}$ to $^4F_{3/2}$. The Er(III) complex **4** shows the most intense bands positioned at 379 and 522 nm that are due to the transitions $^4I_{15/2} \rightarrow ^4G_{11/2}$ and $^4I_{15/2} \rightarrow ^2H_{11/2}$ [49,53-55].

3.3. Coordination geometry analysis

The geometries of the NaO_5 , NaO_6 , LnO_9 and LnO_8 coordination polyhedra of the lanthanide complexes with Hpma^- were evaluated by continuous shape measures using *SHAPE 2.1* software, for quantification of the degree of distortion of the Ln(III) coordination geometry (Table 3). The polyhedral data generated using *VESTA* are presented in Figure 5. For all the coordination compounds, there are no significant distortions from the ideal polyhedra (CShM values ≤ 3) [56-58]. The shape analysis of the nine-coordinate complexes **1** and **2** highlight the coordination geometry of the distorted spherical tricapped trigonal prism (TCTPR-9), with D_{3h} symmetry [59,60]. The Nd(III) complex **2** is closer to the TCTPR-9 geometry than complex **1** with the larger metal Ce(III) ion. The continuous shape measures obtained for the spherical capped square antiprism (CSAPR-9) shape in **1** (CShM = 0.92568) and **2** (CShM = 0.82770), however, exhibit a small difference from the TCTPR-9 geometry [61]. Hence, the coordination spheres of **1** and **2** can be considered as the intermediate between CSAPR-9 and TCTPR-9 geometries [61,62]. The coordination polyhedron of the octa-coordinated Er1 atom of **4** can be viewed as a square antiprism (SAPR-8), with a deviation parameter from the ideal SAPR-8 of 0.43454 [56].

The least CShM parameters for the nine-coordinate Ln(III) ions of **3–6** indicate the distorted CSAPR-9 geometry (C_{4v}). Despite having a similar coordination environment, the Gd(III) coordination polyhedra in **3** display a small difference in CShM values. Distortion parameters are in the order Nd(III) > Gd(III) > Er(III). The other closest geometries for Nd1 (complex **5**) and Gd1 (complex **6**) is TCTPR-9, with deviation values of 0.98091 and 0.86226, respectively; while that of Gd2 (complex **6**) is a muffin geometry (MFF-9) (CShM = 0.93876) [59,61,62]. In addition, the oxygen atoms around the hexa-coordinate Na cations in **5** and **6** form two square-based pyramids, adopting an octahedron (OC-6) shape (CShM values of 1.90099 and 2.08861, respectively), whereas the geometry of the five-coordinate Na ions can be described as vacant octahedron (vOC-5), possessing C_{4v} symmetry [63,64].

There is a better fit to the ideal polyhedra as the atomic number of the $4f$ elements increase, as evidenced by the smaller shape measure values. This is due to the shorter and stronger bonds, as well as decreased room for angular distortions as the metal ions decrease in size [57]. The volume of the coordination polyhedra is controlled by the size of the metal ions, as well as the coordination numbers. Smaller metal ions and lower coordination numbers result in smaller polyhedral volumes. A comparison between the Ln(III) coordination environments of all the complexes reflect the highest polyhedral volume for the nine-coordinate Ce(III) compound (32.4845 Å³), and the smallest polyhedron size for the eight-coordinate Er1 in **4** (22.5763 Å³).

3.4. Crystal structures and hydrogen bonding

The reactions in aqueous mixtures between the lanthanide nitrate salts and Hdmp (Figure 6a), in the presence of NaOH, yield interesting Ln(III)–organic coordination polymers, formulated as: $\{[\text{Ln}(\text{Hpma})_3(\text{MeOH})(\text{H}_2\text{O})] \cdot 2\text{MeOH}\}_n$ (Ln = Ce and Nd), $\{[\text{Gd}_2(\text{Hpma})_6(\text{MeOH})_4] \cdot 6\text{MeOH}\}_n$, $\{[\text{Er}_2(\text{Hpma})_6(\text{MeOH})(\text{H}_2\text{O})_3] \cdot 2\text{MeOH}\}_n$ and $[\text{Ln}_2\text{Na}_2(\text{Hpma})_8(\text{EtOH})(\text{H}_2\text{O})_6]_n$ (Ln = Nd and Gd) (Figures 6b-e; see Tables 4a and 4b for bond parameters). X-ray diffraction studies of the single crystals revealed that the isostructural complexes **1** and **2** crystallise in the monoclinic space groups $I2/a$, whereas complexes **3–6** give the triclinic crystal structure, belonging to the $P-1$ space group. Complexes **5** and **6** are also structurally analogous to each other. The polymeric complexes

feature Ln-Hpma moieties bridged by Hpma⁻, giving one-dimensional (1D) zig-zag chains of the –Ln–O–C–O–Ln– type, with the Ln···Ln separation varying from 6.271 Å (complex **2**) to 6.843 Å (complex **5**), thus showing well isolated mononuclear units (Figure 6f) [65-67]. The chelating and bridging modes of Hpma⁻ *via* only the oxygen atoms are indicated in Figure 6g [68-70].

Three bidentate Hpma⁻ ligands, one methanol and one water molecule form the mononuclear units of **1** and **2**, which are connected through the fourth bridging oxamate ligand (Figure 6b). Complexes **1** and **2** have voids, with the voids of **1** having too little electron density to model anything, whereas the voids of **2** may contain one or two water molecules but are too extensively disordered over a large volume to model. The Ce(III) and Nd(III) ions are nine-coordinate with the oxygen atoms bonded to form a distorted spherical tricapped trigonal prism geometry. Furthermore, there are two non-coordinating methanol molecules present in the lattices.

Complex **3** is characterised by dinuclear units containing similar spherical capped square antiprism GdO₉ cores, with each nona-coordinate environment constructed from three chelating Hpma⁻ ligands, two methanol molecules and one oxygen atom from the bridging (tridentate) Hpma⁻ ligand (Figure 6c). Complex **4** gives metal centres comprising distinct Er(1)O₈ (SAPR-8) and Er(2)O₉ (CSAPR-9) cores linked by chelating/bridging Hpma⁻ ligands (Figure 6d). The Er1 coordination sphere is made up of three bidentately coordinated Hpma⁻ ligands and two water molecules, whilst the nine-coordinate Er2 ion is surrounded by three η^2 -bonded oxamates, one methanol, one water molecule and an *O*-atom from the tridentate Hpma⁻. In addition, the metal complexes **3** and **4** feature lattice methanol solvates (six for complex **3** and two for complex **4**).

Coordination compounds **5** and **6** yielded lanthanide(III)-sodium(I) complexes, with Ln₂Na₂ (Ln = Nd and Gd) cores bridged by the μ_2 - η^1 : η^1 : η^1 , μ_3 - η^1 : η^2 : η^1 and μ_2 - η^1 : η^2 oxamate ligands, as well as by the μ_2 -H₂O oxygen atoms (Figures 6e and 6h) [68-70]. The asymmetric unit contains two nine-coordinate Ln(III) ions with the CSAPR-9 geometry. Complexes **5** and **6** also contain voids with enough electron density to contain one ethanol and water molecule (and their inversion symmetries). One extensively disordered ethanol molecule has been modelled. The Ln1 atom is surrounded by three η^2 Hpma⁻, two *O*-atoms from the bidentately coordinated μ_2 - η^1 : η^2 Hpma⁻ and one oxygen provided by μ_3 - η^1 : η^2 : η^1 bonded Hpma⁻, whereas

the O₉ donor-set of Ln2 is fulfilled with six oxygen atoms from *O,O*-donor oxamate ligands (O52, O53, O61, O62, O71, O72), two oxygen atoms from a bridging Hpma⁻ and a μ₂-O bridging water molecule. Each Na1 is in a hexa-coordinate environment, linked to four μ₂-O atoms of water, and two oxygen atoms from the μ₂-η¹:η² and the μ₃-η¹:η²:η¹ Hpma⁻, while the vacant octahedron geometry of Na2 is constructed from five *O*-atoms (two H₂O molecules, one μ₂-O_{water}, one disordered ethanol and one bridging oxygen of Hpma⁻). The crystal structures of the heterometallic complexes feature rhomboidal Ln-O-Na-O cores, where bridging occurs through the *O*-atoms of Hpma⁻ and water molecules, having bridging oxygen atoms lying almost equidistant between the metal ions [the M-O_{Hpma-} and M-O_{water} (M = Nd, Gd and Na) bonds vary from 2.3771(16) to 2.469(2) and from 2.5143(16) to 2.566(2) Å, respectively] [71]. The O-M-O, Ln-O_{water}-Na and Ln-O_{Hpma-}-Na bond angles in these rhomboids are in the ranges 65.85(6)–67.01(5), 107.63(7)–108.05(7) and 117.17(8)–117.20(7) °, respectively. The Ln-O_{water}-Na bond angles do not display any anomalies and compare well with the 108.66(9) ° Gd–O–Gd angle in [Gd₂(bfa)₄L₂]CH₂Cl₂ (bfa = benzoyltrifluoroacetone and HL = 2-[[[(4-methylphenyl)imino]methyl]-8-hydroxyquinoline) [72]. The Na(I) ions are connected to each other *via* the water oxygen atoms, with Na1–O_{water}–Na2 angles of 120.31(9) ° (complex **5**) and 121.16(8) ° (complex **6**).

All the metal complexes are comprised of bidentately (η²) coordinated Hpma⁻ ligands, leading to five-membered chelate rings with O-Ln-O angles of 63.51(4)–69.80(6) ° and Ln-O_{Hpma-} distances of 2.2722(18)–2.4752(12) Å, which are comparable to those in the previously reported dysprosium(III) complex containing *N*-(2,6-dimethylphenyl) oxamic acid [Dy-O bond lengths = 2.340(2)–2.407(2) Å; O-Dy-O bite angles = 67.36(8) to 68.04(7) °] (Tables 4a and 4b) [15]. The shortening of the C4-O2 bond [1.3138(17) Å] of Hdmp in the complexes [e.g. O12-C19 = 1.2564(19) Å in **1**] suggest a double bond character in the Hpma⁻ ligand, as a result of delocalisation across the oxamate moiety [73]. The Ln-O_{water} and Ln-O_{MeOH} distances, spanning the ranges 2.3369(19)–2.5049(13) and 2.391(2)–2.5404(12) Å, respectively, are similar to those in the triaqua[2,6-diacetylpyridine bis(benzoylhydrazon)]methanol-lanthanide(III) complexes reported by Kachi-Terajima *et al.* (2018) [Ln-O_{water} = 2.313(2)–2.428(2) and Ln-O_{MeOH} = 2.472(2)–2.4867(18) Å, Ln = Tb and Dy] [74]. The Na-O_{oxamate} bond lengths of **5** and **6** [spanning the range 2.336(2)–2.476(2) Å], compare well with the bond parameters of the alkaline salts of bis(oxamato)palladate(II) complexes reported by Fortea-Pérez *et al.* (2014) [Na-O_{oxamate} = 2.273(5)–2.909(5) Å] [75]. A

decrease in the Ln-O distances with increasing atomic number is observed, as expected due to the result of the lanthanide contraction [66,70,76].

The crystal structures of **1–6** are further stabilised by networks of medium strength hydrogen bonds of the N-H \cdots O and O-H \cdots O type, as presented in Figure 6i and Table 4c [59,77-79]. Only intermolecular N-H \cdots O bonds [H \cdots O = 2.232(17)–2.408(17) Å] are found in the proligand, which are satisfied by the amide N-H groups of one molecule and the oxygen atoms of the oxamate group from a neighbouring molecule. It is important to note that these hydrogen bond interactions in the metal complexes involve the crystallographic methanol solvent molecules and have *DA* (Donor \cdots Acceptor) distances in the range 2.644(3)–3.183(3) Å. N-H \cdots O bonds are apparent between the amide N-H (donor) and the solvent molecules or the O-atoms of Hpma $^-$ as acceptors. As observed in **1** and **2**, the two lattice methanol solvent molecules, along with the coordinated water and the bonded oxygen atoms of Hpma $^-$, play a key role in establishing O-H \cdots O interactions. In **3**, the methanol molecules in the primary and secondary coordination spheres act as donors, assuring connectivity with the oxygen atoms of the oxamate ligands. As shown in Figure 6i, the coordinated water molecules of **4** form hydrogen bonds with the lattice methanol molecules, for example O2-H2A \cdots O5 with a *DA* distance of 2.663(3) Å. The crystal structures of the heterometallic complexes **5** and **6** are also stabilised by a variety of hydrogen bonds, some of which involve monodentate and bridging water molecules as hydrogen donors and oxamate oxygen atoms as acceptors. The crystal packing of the metal complexes is supplemented by weak contacts: C-H_{Hpma} \cdots O_{Hpma} $^-$ (**1–6**), C-H_{MeOH} \cdots O_{Hpma} $^-$ (**2–4**), C-H_{Hpma} \cdots O_{MeOH} (**3**), C-H_{MeOH} \cdots O_{MeOH} (**4**), C-H_{Hpma} \cdots O_{H2O} (**5**), as well as C-H_{Hpma} \cdots N_{Hpma} $^-$ (**5** and **6**) [80].

3.5. Atomic charge analysis of the ligand and MEP surface

The total atomic charges of the anionic oxamate ligands were determined by the NPA method, and are presented in graphical form, shown in Figure 7b (see Figure 7a for atom-numbering) [81]. According to the NPA method, the obtained atomic charges indicate that the C22, C23 and H24 atoms have larger positive atomic charges compared to the other hydrogen atoms. Atoms O1, O2 and O3 exhibit the most negative atomic charges (-0.6720, -0.76420 and -0.79536 in DMSO). Natural population analysis predicted the same tendencies on the net atomic charges of the aforementioned atoms in the gas phase, with the charges on

O1, O2 and O3 being -0.63226, -0.70104 and -0.78570, respectively. This explains the ability of the atoms to network with the positively-charged component, with O3 having a stronger coordination ability to form stronger (shorter) Ln-O bonds [82]. The calculated results thus concur with most of the experimental Ln-O_{oxamate} results obtained through the X-ray diffraction studies. The nitrogen atom N4 displays an electronegativity (-0.63544 in DMSO and -0.67626 in the gas phase) lower than that of the oxygen atoms. The electronegative O-atoms therefore have the tendency to donate electrons, while the electropositive carbon and hydrogen atoms have a tendency to accept electrons [81,83,84]. The presence of large negative charges on the oxygen and nitrogen atoms, and positive charges on the hydrogen atoms suggest the possibility of intermolecular interactions in the crystal structure [85].

The accrual of charges on selected atoms and the distribution of electrons in the core, valence and Rydberg sub-shells of Hpma⁻, are shown in Table 5. Furthermore, NPA in solvent shows that 102 electrons in the ligand have the sub-shell distributions as follows:

Core:	27.99986 (99.9995% of 28)
Valence:	73.60526 (99.4666% of 74)
Rydberg:	0.39488 (0.3871% of 102)

Molecular electrostatic potential (MEP) mapping was applied in the interpretation and prediction of the reactive behaviour of Hpma⁻ in nucleophilic and electrophilic reactions, as well as in depicting the shape of the oxamate ligand (Figure 7c) [81,86]. This is important in predicting chemical reactivities in hydrogen bond interactions and biological systems [26]. The oxygen atoms of Hpma⁻ are associated with a strong negative molecular electrostatic potential region. The concentration of maximum electron density on the oxygen atoms enables interaction with trivalent metal ions to form *O,O*-donor chelates, as well as the participation of the remaining *O*-atom in bridging. In addition to bonding with Ln(III) ions, the MEP region around the oxygen atoms suggest that these oxygen atoms can also act as hydrogen bond acceptors, which is consistent with the X-ray analysis. The nitrogen atom comparatively possesses a smaller negative MEP region.

3.6. Global and chemical reactivity descriptors

Some of the most imperative parameters for biological chemistry, chemical reactivity and drug design, like the *HOMO*, *LUMO* and the *HOMO-LUMO* gaps of Hpma⁻, were calculated using the basis set B3LYP/aug-cc-pVTZ and visualised from the computed data using *Avogadro* software (Figure 8 and Table 6) [87]. The *HOMO*, *HOMO-1* (second highest) and *HOMO-2* (third highest) energies in order are -6.233, -6.554 and -6.654 eV, whereas the *LUMO*, *LUMO+1* (second lowest) and *LUMO+2* (third lowest) were calculated to be -0.784, -0.339 and -0.245 eV, respectively. The observed energy gaps pertaining to the energy needed to achieve electronic transitions between the *HOMO-LUMO*, *HOMO-1-LUMO+1* and *HOMO-2-LUMO+2* are 5.449, 6.215 and 6.409 eV, respectively. These energy gaps play an important role in the elucidation of the chemical stability of a molecule, with a highly stable molecule depicted by a high energy gap, and a low energy gap being typical of high reactivity [87,88]. The ionisation potential ($I = -E_{HOMO} = 6.233$ eV) and electron affinity ($A = -E_{LUMO} = 0.784$ eV) are predictable from the *HOMO* and *LUMO* energy values [87].

Global reactivity descriptors, such as chemical potential (μ), hardness (η), softness (σ), electrophilicity index (ω) and electronegativity (χ_m), were determined by resorting to the ionisation potential and electron affinity obtained from the *HOMO* and *LUMO* energies, with the results being $\mu = -3.509$ eV, $\eta = 2.725$ eV, $\sigma = 0.367$ eV⁻¹, $\omega = 2.259$ eV and $\chi_m = 3.509$ eV [87,88]. These parameters are an efficient tool in providing theoretical insights into the biological activity and behaviour of the whole chemical species when the compound enters the body as an anticancer drug [89,90]. Calculations for the local reactivity parameters: electrodonating (ω^-) power, electroaccepting (ω^+) power and the net electrophilicity ($\Delta\omega^\pm$), are also included (Table 6) to provide information regarding the behaviour of specific sites in the molecule, which is crucial in reactivity elucidation and selectivity trends [91-93]. The electrodonating power ($\omega^- = 4.354$ eV) shows the propensity to donate charge, whereas the electroaccepting capacity ($\omega^+ = 0.845$ eV) indicates the tendency of a system to accept charge; with the ω^- value of the molecule being more important than its electroaccepting ability [92-94]. The net electrophilicity (electron-accepting ability relative to its electron-donating capacity) is equal to 5.199 eV [95].

3.7. Anticancer studies

The viability of MCF-7, HEC-1A and THP-1 cells was determined after exposure to 100 μM of the proligand Hdmp, Ln(III) nitrate salts, Ln(III) oxamate complexes and curcumin, for 24 hours. As shown in Figure 9, the results indicate that when exposed to $[\text{Ce}(\text{NO}_3)_3 \cdot 6\text{H}_2\text{O}]$, the cell viability of the MCF-7 cells decreased ($p < 0.05$). Likewise, $[\text{Nd}(\text{NO}_3)_3 \cdot 6\text{H}_2\text{O}]$ exerted cytotoxic effects in HEC-1A cells ($p < 0.05$). The cytotoxicities of Hdmp, $[\text{Ln}(\text{NO}_3)_3 \cdot x\text{H}_2\text{O}]$ (Ln = Gd and Er) and metal complexes **1–6** were also tested against the three cell lines for comparison, but no significant cytotoxicity was noted ($p > 0.05$).

The greatest cytotoxic effect was observed after exposure to curcumin, which decreased cell viabilities to 46.8 ± 6.46 , 14.1 ± 3.76 and $21.5 \pm 0.83\%$ for MCF-7, HEC-1A and THP-1 cells, respectively. The cytotoxicity of curcumin is explicated by its ability to regulate multiple cell signalling pathways, such as cell proliferation, senescence, apoptosis and the protein kinase pathway [34,96].

For each assay, the viability of the THP-1 cells treated with the proligand, lanthanide salts and the coordination compounds were not significantly affected, suggesting no adverse effects on THP-1 cell line counterparts, *i.e.* primary monocytes or human peripheral blood monocytes (Figure 9) [97-99]. This, however, needs to be validated by further *in vitro* and *in vivo* studies.

4. Summary

Syntheses of six novel oxamates of trivalent rare-earth metals (Ce, Nd, Gd and Er) in basic media have been successfully reported. The compositions and structures of these polymeric complexes have been characterised by elemental analyses, conductivity measurements, IR, UV-Vis-NIR, NMR and X-ray diffraction studies. The X-ray crystallography results indicate that the Hpma^- ligand possesses a variety of chelating and bridging modes, displayed by the three oxygen atoms. The units of **1–4** contain lattice methanol molecules, which afford oxygen atoms needed in the formation of some O-H \cdots O links. The oxamate ligands adopt the μ_2^- and μ_3^- -bridging modes, generating one-dimensional coordination polymers. In the heterometallic polymers **5** and **6**, interconnection of Ln(III) and Na(I) ion centres is also supplemented by μ_2^- -bridging water molecules. The experimental bond parameters were in excellent agreement with related compounds in the literature.

Using the B3LYP/aug-cc-pVTZ level, NPA of *N*-(2,6-dimethylphenyl)oxamate has been performed to evaluate partial atomic charges. The *HOMO* and *LUMO* energies, as well as the MEP surfaces, assisted in determining the chemical reactivity of the title anionic ligand. Partial atomic charges and MEP surfaces of the oxamate ligand are corroborated by the crystal data.

An MTT assay was employed to determine MCF-7, HEC-1A and THP-1 viability after exposure to 100 μ M of the compounds, by determining the reduction of MTT to formazan crystals. Although no evidence of cytotoxicity was observed for the title complexes, the rare-earth metal salts [Ce(NO₃)₃·6H₂O] and [Nd(NO₃)₃·6H₂O] showed modest cytotoxicity against MCF-7 and HEC-1A cells, respectively. Complexes **2** and **3** also show cytotoxicity against HEC-1A. These results indicate that these two metal salts could be potential starting materials in the development of anticancer agents. Further attempts will be concentrated on the preparation of other complexes from Hdmp or Hpma⁻ derivatives.

Acknowledgements

Funding from the National Research Foundation (unique grant number: 106004) and Nelson Mandela University Postgraduate Research Scholarship is gratefully acknowledged. The authors would like to thank the Centre for High Performance Computing of South Africa, for allowing access to usage of computational resources to execute this research. The authors also thank the supportive experimental assistance of Mr Kwakhanya Mkwakwi, Mr Cameron Matthews and Mr Cyprian Moyo from Nelson Mandela University.

Appendix A. Supplementary data

Crystallographic data for the reported complexes have been deposited at the Cambridge Crystallographic Data Centre with CCDC reference numbers 1985517–1985523. These data are available from the CCDC, 12 Union Road, Cambridge CB2 1EZ, UK on request or can be obtained free of charge from the Cambridge Crystallographic Data Center *via* https://www.ccdc.cam.ac.uk/data_request/cif.

References

- [1] American Cancer Society. *Global Cancer Facts & Figures*, 3rd Edition, Atlanta: American Cancer Society; 2015, pp. 1–10.
- [2] R. Shah, K. Rosso, S.D. Nathanson, “Pathogenesis, prevention, diagnosis and treatment of breast cancer”, *World J. Clin. Oncol.*, **5** (2014) 283–284.
- [3] M.I. Nounou, F. ElAmrawy, N. Ahmed, K. Abdelraouf, S. Goda, H. Syed-Sha-Qhattal, “Breast Cancer: Conventional diagnosis and treatment modalities and recent patents and technologies”, *Breast Cancer: Basic and Clinical Research*, **9** (2015) 17–34.
- [4] A. Talhouk, J.N. McAlpine, “New classification of endometrial cancers: The development and potential applications of genomic-based classification in research and clinical care”, *Gynecologic Oncology Research and Practice*, **3** (2016) 1–12.
- [5] X. Wang, M. Yan, Q. Wang, H. Wang, Z. Wang, J. Zhao, J. Li, Z. Zhang, “*In vitro* DNA-binding, anti-oxidant and anticancer activity of indole-2-carboxylic acid dinuclear copper(II) complexes”, *Molecules*, **22** (2017) 1–13.
- [6] Y. Ellahioui, S. Prashar, S. Gómez-Ruiz, “Anticancer applications and recent investigations of metallodrugs based on gallium, tin and titanium”, *Inorganics*, **5** (2017) 1–23.
- [7] K. Wang, R. Li, Yi Cheng, B. Zhu, “Lanthanides – the future drugs?”, *Coord. Chem. Rev.*, **190–192** (1999) 297–308.
- [8] I. Kostova, “Lanthanides as anticancer agents”, *Curr. Med. Chem. – Anti-Cancer Agents*, **5** (2005) 591–602.
- [9] S.P. Perlepes, T.F. Zafiropoulos, J.K. Kouinis, A.G. Galinos, “Lanthanide(III) complexes of oxamic acid”, *Z. Naturforsch.*, **36b** (1981) 697–703.
- [10] Z. Zhao, F. Han, S. Yang, J. Wu, W. Zhan, “Oxamate-mediated inhibition of lactate dehydrogenase induces protective autophagy in gastric cancer cells: Involvement of the Akt–mTOR signaling pathway”, *Cancer Lett.*, **358** (2015) 17–26.
- [11] C.J. Valvona, H.L. Fillmore, “Oxamate, but not selective targeting of LDH-A, inhibits medulloblastoma cell glycolysis, growth and motility”, *Brain Sci.*, **8** (2018) 1–12.
- [12] Y. Yang, D. Su, L. Zhao, D. Zhang, J. Xu, J. Wan, S. Fan, M. Chen, “Different effects of LDH-A inhibition by oxamate in non-small cell lung cancer cells”, *Oncotarget*, **5** (2014) 11886–11895.
- [13] F.J. Caires, W.D.G. Nunes, C. Gaglieri, A.L.C.S. do Nascimento, J.A. Teixeira, G.A.C. Zangaro, O. Treu-Filho, M. Ionashiro, “Thermoanalytical, spectroscopic and DFT studies of heavy trivalent lanthanides and yttrium(III) with oxamate as ligand”, *Mater. Res.*, **20** (2017) 937–944.

- [14] R.D. Teo, J. Termini, H.B. Gray, “Lanthanides: Applications in cancer diagnosis and therapy”, *J. Med. Chem.*, **59** (2016) 6012–6024.
- [15] F.R. Fortea-Pérez, J. Vallejo, M. Julve, F. Lloret, G. De Munno, D. Armentano, E. Pardo, “Slow magnetic relaxation in a hydrogen-bonded 2D array of mononuclear dysprosium(III) oxamates”, *Inorg. Chem.*, **52** (2013) 4777–4779.
- [16] M.V. Berridge, A.S. Tan, “Characterization of the cellular reduction of 3-(4,5-dimethylthiazol-2yl)-2,5-diphenyltetrazolium bromide (MTT): subcellular localization, substrate dependence, and involvement of mitochondrial electron transport in MTT reduction”, *Arch. Biochem. Biophys.*, **303** (1993) 474–482.
- [17] A. Bahuguna, I. Khan, V.K. Bajpai, S.-C. Kang, “MTT assay to evaluate the cytotoxic potential of a drug”, *Bangladesh J. Pharmacol.*, **12** (2017) 115–118.
- [18] L.J. Farrugia, “WinGX and ORTEP for Windows: an update”, *J. Appl. Crystallogr.*, **45** (2012) 849–854.
- [19] C.F. Macrae, I.J. Bruno, J.A. Chisholm, P.R. Edgington, P. McCabe, E. Pidcock, L. Rodriguez-Monge, R. Taylor, J. van de Streek, P.A. Wood, “Mercury CSD 2.0 – new features for the visualization and investigation of crystal structures”, *J. Appl. Crystallogr.*, **41** (2008) 466–470.
- [20] M. Pinsky, D. Avnir, “Continuous Symmetry Measures. 5. The Classical Polyhedra”, *Inorg. Chem.*, **37** (1998) 5575–5582.
- [21] K. Momma, F. Izumi, “VESTA 3 for three-dimensional visualization of crystal, volumetric and morphology data”, *J. Appl. Crystallogr.*, **44** (2011) 1272–1276.
- [22] Bruker. APEX2, SAINT and SADABS. Bruker AXS Inc., Madison, WI, USA (2004).
- [23] G.M. Sheldrick, “SHELXT – Integrated space-group and crystal structure determination”, *Acta Cryst.*, **A71** (2015) 3–8.
- [24] G.M. Sheldrick, “Crystal structure refinement with SHELXL”, *Acta Cryst.*, **C71** (2015) 3–8.
- [25] C.B. Hübschle, G.M. Sheldrick, B. Dittrich, “ShelXle: a Qt graphical user interface for SHELXL”, *J. Appl. Cryst.*, **44** (2011) 1281–1284.
- [26] M.S. Alam, D.-U. Lee, “Syntheses, crystal structure, Hirshfeld surfaces, fluorescence properties, and DFT analysis of benzoic acid hydrazone Schiff bases”, *Spectrochim. Acta Part A*, **145** (2015) 563–574.
- [27] R.A. Kendall, T.H. Dunning, R.J. Harrison, “Electron affinities of the first-row atoms revisited. Systematic basis sets and wave functions”, *J. Chem. Phys.*, **96** (1992) 6796–6806.

- [28] E.D. Glendening, J.K. Badenhop, A.E. Reed, J.E. Carpenter, J.A. Bohmann, C.M. Morales, C.R. Landis, F. Weinhold, Theoretical Chemistry Institute, University of Wisconsin, Madison, WI, (2013); <http://nbo6.chem.wisc.edu/>
- [29] E.D. Glendening, C.R. Landis, F. Weinhold, "NBO 6.0: Natural Bond Orbital Analysis Program", *J. Comput. Chem.*, **34** (2013) 1429–1437.
- [30] N.K. Nobel, K. Bamba, O.W. Patrice, N. Ziao, "NBO population analysis and electronic calculation of four azopyridine ruthenium complexes by DFT method", *Computational Chemistry*, **5** (2017) 51–64.
- [31] C. Theivarasu, R. Murugesan, "Natural Bond Orbital (NBO) population analysis of an energetic molecule 1-phenyl-2-nitroguanidine", *Int. J. Chem. Sci.*, **14** (2016) 2029–2050.
- [32] C.B. Hübschle, B. Dittrich, "MoleCoolQt - a molecule viewer for charge-density research", *J. Appl. Cryst.*, **44** (2011) 238–240.
- [33] R. Wilken, M.S. Veena, M.B. Wang, E.S. Srivatsan, "Curcumin: A review of anti-cancer properties and therapeutic activity in head and neck squamous cell carcinoma", *Mol. Cancer*, **10** (2011) 2–19.
- [34] J. Ravindran, S. Prasad, B.B. Aggarwal, "Curcumin and cancer cells: How many ways can curry kill tumor cells selectively?", *AAPS J.*, **11** (2009) 495–510.
- [35] B.A. Avelar-Freitas, V.G. Almeida, M.C.X. Pinto, F.A.G. Mourão, A.R. Massensini, O.A. Martins-Filho, E. Rocha-Vieira, G.E.A. Brito-Melo, "Trypan blue exclusion assay by flow cytometry", *Braz. J. Med. Biol. Res.*, **47** (2014) 307–315.
- [36] C.W. Wright, S.I. Melwani, J.D. Phillipson, D.C. Warhurst, "Determination of anti-giardial activity *in vitro* by means of soluble formazan production", *Trans. R. Soc. Trop. Med. Hyg.*, **86** (1992) 517–519.
- [37] Z.-Q. Xu, X.-J. Mao, L. Jia, J. Xu, T.-F. Zhu, H.-X. Cai, H.-Y. Bie, R.-H. Chen, T.-L. Ma, "Synthesis, characterization and anticancer activities of two lanthanide(III) complexes with a nicotinohydrazone ligand", *J. Mol. Struct.*, **1102** (2015) 86–90.
- [38] F.R. Fortea-Pérez, D. Armentano, M. Julve, G. De Munno, S.-E. Stiriba, "Bis(oxamato)palladate(II) complexes: synthesis, crystal structure and application to catalytic Suzuki reaction", *J. Coord. Chem.*, **67** (2014) 4003–4015.
- [39] Z.A. Taha, A.M. Ajlouni, T.S. Ababneh, W. Al-Momani, A.K. Hijazi, M. Al Masri, H. Hammad, "DFT computational studies, biological and antioxidant activities, and kinetics of thermal decomposition of 1,10-phenanthroline lanthanide complexes", *Struct. Chem.*, **28** (2017) 1907–1918.
- [40] L. Pavelek, V. Ladányi, M. Nečas, Z. Moravec, K. Wichterle, "Synthesis and characterization of lanthanide complexes with a pentadentate triazine-based ligand", *Polyhedron*, **119** (2016) 134–141.

- [41] X. Feng, L.-L. Zhou, L.-Y. Wang, J.-G. Zhou, Z.-Q. Shi, J.-J. Shang, "Two unique lanthanide–organic frameworks based on 1*H*-2-methyl-4,5-imidazole-dicarboxylate and oxalate: Crystal structure, luminescence and magnetic properties", *Inorg. Chim. Acta*, **394** (2013) 696–702.
- [42] G.-C. Zong, J.-X. Huo, N. Ren, J.-J. Zhang, X.-X. Qi, J. Gao, L.-N. Geng, S.-P. Wang, S.-K. Shi, "Preparation, characterization and properties of four new trivalent lanthanide complexes constructed using 2-bromine-5-methoxybenzoic acid and 1,10-phenanthroline", *Dalton Trans.*, **44** (2015) 14877–14885.
- [43] L.-N. Sun, H.-J. Zhang, Q.-G. Meng, F.-Y. Liu, L.-S. Fu, C.-Y. Peng, J.-B. Yu, G.-L. Zheng, S.-B. Wang, "Near-infrared luminescent hybrid materials doped with lanthanide (Ln) complexes (Ln = Nd, Yb) and their possible laser application", *J. Phys. Chem. B*, **109** (2005) 6174–6182.
- [44] E.J. Shiells, L.S. Natrajan, D. Sykes, M. Tropicano, P. Cooper, A.M. Kenwright, S. Faulkner, "Lanthanide complexes of DOTA monoamide derivatives bearing an isophthalate pendent arm", *Dalton Trans.*, **40** (2011) 11451–11457.
- [45] C.J. Athira, Y. Sindhu, M.S. Sujamol, K. Mohanan, "Synthesis and spectroscopic characterization of some lanthanide(III) nitrate complexes of ethyl 2-[2-(1-acetyl-2-oxopropyl)azo]-4,5-dimethyl-3-thiophenecarboxyate", *J. Serb. Chem. Soc.*, **76** (2011) 249–261.
- [46] R.K. Agarwal, S. Prasad, R. Garg, S.K. Sidhu, "Synthesis and preliminary structural characterization of some lanthanide(III) semicarbazone complexes", *Bull. Chem. Soc. Ethiop.*, **20** (2006) 167–172.
- [47] R.K. Agarwal, A. Kumar, "Synthesis, physico-chemical and biological properties of some mixed ligand complexes of trivalent lanthanides with 4[*N*-(4'-dimethylamino-benzalidene)amino] antipyrine thiosemicarbazone and pyridine", *J. Appl. Chem. Res.*, **16** (2011) 40–58.
- [48] K. Raja, A. Suseelamma, K.H. Reddy, "Synthesis, spectral properties, DNA binding interactions and DNA cleavage studies of lanthanide(III) complexes of 2-acetylpyridine acetylhydrazone: The X-ray crystal structure of 10-coordinate Ce(III) and Sm(III) complexes", *J. Iran Chem. Soc.*, **12** (2015) 1473–1486.
- [49] N. Guskos, J. Majszczyk, J. Typek, G. Zolnierkiewicz, E. Tomaszewicz, K. Aidinis, "Relative intensities of *f-f* transitions of erbium(III) ion studied by photoacoustic spectroscopy", *Rev. Adv. Mater. Sci.*, **23** (2010) 97–101.
- [50] R.K. Agarwal, R.K. Garg, S.K. Sindhu, "Synthesis and magneto-spectral investigations of some six and nine coordinated complexes of lanthanide(III) derived from 4[*N*-(2'-hydroxy-1'-naphthalidene)amino]antipyrinethiosemicarbazone", *J. Iran Chem. Soc.*, **2** (2005) 203–211.
- [51] S. Mohan, K.S. Thind, G. Sharma, "Effect of Nd³⁺ concentration on the physical and absorption properties of sodium-lead-borate glasses", *Braz. J. Phys.*, **37** (2007) 1306–1313.

- [52] L.B. Su, Q.G. Wang, H.J. Li, G. Brasse, P. Camy, J.L. Doualan, A. Braud, R. Moncorgé, Y.Y. Zhan, L.H. Zheng, X.B. Qian, J. Xu, "Spectroscopic properties and CW laser operation of Nd,Y-codoped CaF₂ single crystals", *Laser Phys. Lett.*, **10** (2013) 1–4.
- [53] K.A. Thiakou, V. Nastopoulos, A. Terzis, C.P. Raptopoulou, S.P. Perlepes, "Di-2-pyridyl ketone in lanthanide(III) chemistry: Mononuclear and dinuclear erbium(III) complexes", *Polyhedron*, **25** (2006) 539–549.
- [54] W. Ma, L. Su, X. Xu, J. Wang, D. Jiang, L. Zheng, X. Fan, C. Li, J. Liu, J. Xu, "Effect of erbium concentration on spectroscopic properties and 2.79 μm laser performance of Er:CaF₂ crystals", *Opt. Mater. Express*, **6** (2016) 409–415.
- [55] P. Martin-Ramos, M. Ramos-Silva, F. Lahoz, I.R. Martin, P. Chamorro-Posada, M.E.S. Eusebio, V. Lavin, J. Martin-Gil, "Highly fluorinated erbium(III) complexes for emission in the C-band", *J. Photochem. Photobiol. A*, **292** (2014) 16–25.
- [56] K. Liu, H. Li, X. Zhang, W. Shi, P. Cheng, "Constraining and tuning the coordination geometry of a lanthanide ion in metal–organic frameworks: Approach toward a single-molecule magnet", *Inorg. Chem.*, **54** (2015) 10224–10231.
- [57] J. Cirera, E. Ruiz, S. Alvarez, "Continuous Shape Measures as a stereochemical tool in organometallic chemistry", *Organometallics*, **24** (2005) 1556–1562.
- [58] T. Zhu, P. Chen, H. Li, W. Sun, T. Gao, P. Yan, "Structural effects on the photophysical properties of mono- β -diketonate and bis- β -diketonate Eu^{III} complexes", *Phys. Chem. Chem. Phys.*, **17** (2015) 16136–16144.
- [59] M.N. Gueye, M. Dieng, I.E. Thiam, D. Lo, A.H. Barry, M. Gaye, P. Retailleau, "Lanthanide(III) complexes with tridentate Schiff base ligand, antioxidant activity and X-ray crystal structures of the Nd(III) and Sm(III) complexes", *S. Afr. J. Chem.*, **70** (2017) 8–15.
- [60] H.R. Suh, H.S. Suh, S.S. Yun, E.K. Lee, S.K. Kang, "Triaquateris(2,6-dinitrophenolato)neodymium(III)", *Acta Cryst.*, **E58** (2002) m284–m286.
- [61] S.P. Petrosyants, A.B. Ilyukhin, A.V. Gavrikov, Y.A. Mikhlina, L.N. Puntus, E.A. Varaksina, N.N. Efimov, V.M. Novotortsev, "Luminescent and magnetic properties of mononuclear lanthanide thiocyanates with terpyridine as auxiliary ligand", *Inorg. Chim. Acta*, **486** (2019) 499–505.
- [62] X. Wang, M. Zhu, J. Wang, L. Li, "Unusual Gd–nitronyl nitroxide antiferromagnetic coupling and slow magnetic relaxation in the corresponding Tb analogue", *Dalton Trans.*, **44** (2015) 13890–13896.
- [63] L. Kayser, R. Pattacini, G. Rogez, P. Braunstein, "Nuclearity of nickel and mixed sodium–nickel complexes: dependence on the spacer in chelating pyridine-alcoholate ligands", *Chem. Commun.*, **46** (2010) 6461–6463.

- [64] M.A. Palacios, J. Morlieras, J.M. Herrera, A.J. Mota, E.K. Brechin, S. Triki, E. Colacio, "Synthetic ability of dinuclear mesocates containing 1,3-bis(diazinecarboxamide)benzene bridging ligands to form complexes of increased nuclearity. Crystal structures, magnetic properties and theoretical studies", *Dalton Trans.*, **46** (2017) 10469–10483.
- [65] M. Stolárová, J. Černák, M. Tomás, I. Ara, M. Orendáč, L.R. Falvello, "Two novel coordination polymers in the family of lanthanide complexes with *o*-phenylenedioxydiacetato as ligand", *Polyhedron*, **88** (2015) 149–155.
- [66] D.N. Bazhin, Y.S. Kudyakova, A.S. Bogomyakov, P.A. Slepukhin, G.A. Kim, Y.V. Burgart, V.I. Saloutin, "Dinuclear lanthanide–lithium complexes based on fluorinated β -diketonate with acetal group: magnetism and effect of crystal packing on mechanoluminescence", *Inorg. Chem. Front.*, **6** (2019) 40–49.
- [67] M.-S. Liu, Q.-Y. Yu, Y.-P. Cai, C.-Y. Su, X.-M. Lin, X.-X. Zhou, J.-W. Cai, "One-, two-, and three-dimensional lanthanide complexes constructed from pyridine-2,6-dicarboxylic acid and oxalic acid ligands", *Cryst. Growth Des.*, **8** (2008) 4083–4091.
- [68] Z. Feng, X. Zhu, S. Wang, S. Wang, S. Zhou, Y. Wei, G. Zhang, B. Deng, X. Mu, "Synthesis, structure, and reactivity of lanthanide complexes incorporating indolyl ligands in novel hapticities", *Inorg. Chem.*, **52** (2013) 9549–9556.
- [69] Y.-H. Luo, F.-X. Yue, X.-Y. Yu, X. Chen, H. Zhang, "Coordination polymers of lanthanide complexes with benzene dicarboxylato ligands", *CrystEngComm.*, **15** (2013) 6340–6348.
- [70] C. Huang, *Rare-Earth Coordination Chemistry – Fundamentals and Applications*, John Wiley & Sons, Asia, 2010, pp. 91–229.
- [71] K. Shen, Y. Diskin-Posner, L.J.W. Shimon, G. Leitus, R. Carmieli, R. Neumann, "Aerobic oxygenation catalyzed by first row transition metal complexes coordinated by tetradentate mono-carbon bridged bisphenanthroline ligands: intra- versus intermolecular carbon–hydrogen bond activation", *Dalton Trans.*, **48** (2019) 6396–6407.
- [72] W.-M. Wang, W.-W Duan, L.-C. Yue, Y.-L. Wang, W.-Y. Ji, C.-F. Zhang, M. Fang, Z.-L. Wu, "Magnetic refrigeration and single-molecule magnet behaviour of two lanthanide dinuclear complexes (Ln = Gd^{III}, Tb^{III}) based on 8-hydroxyquinolin derivatives", *Inorg. Chim. Acta*, **466** (2017) 145–150.
- [73] M.W. Drover, J.A. Love, L.L. Schafer, "1,3-*N,O*-complexes of late transition metals. Ligands with flexible bonding modes and reaction profiles", *Chem. Soc. Rev.*, **46** (2017) 2913–2940.
- [74] C. Kachi-Terajima, N. Kimura, "Crystal structures of two isotypic lanthanide(III) complexes: triaqua[2,6-diacetylpyridine bis(benzoylhydrazone)]methanollanthanide(III) trichloride methanol disolvates (Ln^{III} = Tb and Dy)", *Acta Cryst.*, **E74** (2018) 535–538.

- [75] F.R. Fortea-Pérez, N. Marino, D. Armentano, G. De Munno, M. Julve, S.-E. Stiriba, “Solid-state *cis-trans* isomerism in bis(oxamato)palladate(II) complexes: synthesis, structural studies and catalytic activity”, *CrystEngComm.*, **16** (2014) 6971–6988.
- [76] R. Ilmi, K. Iftikhar, “Structure elucidation by sparkle/RM1, effect of lanthanide contraction and photophysical properties of lanthanide(III) trifluoroacetylacetonate complexes with 1,10-phenanthroline”, *J. Photochem. Photobio. A*, **325** (2016) 68–82.
- [77] S. Ullmann, P. Hahn, L. Blömer, A. Mehnert, C. Laube, B. Abel, B. Kersting, “Dinuclear lanthanide complexes supported by a hybrid salicylaldiminato/calix[4]arene-ligand: synthesis, structure, and magnetic and luminescence properties of (HNEt₃)[Ln₂(HL)(L)] (Ln = Sm^{III}, Eu^{III}, Gd^{III}, Tb^{III})”, *Dalton Trans.*, **48** (2019) 3893–3905.
- [78] J. Vančo, Z. Trávníček, O. Kozák, R. Boča, “Structural, magnetic and luminescent properties of lanthanide complexes with *N*-salicylidene-glycine”, *Int. J. Mol. Sci.*, **16** (2015) 9520–9539.
- [79] L. Puntus, K. Zhuravlev, K. Lyssenko, M. Antipin, I. Pekareva, “Luminescence and structural properties of lanthanide complexes of Schiff bases derived from pyridoxal and amino acids”, *Dalton Trans.*, **36** (2007) 4079–4088.
- [80] Y. Gu, T. Kar, S. Scheiner, “Fundamental properties of the CH \cdots O interaction: Is it a true hydrogen bond?”, *J. Am. Chem. Soc.*, **121** (1999) 9411–9422.
- [81] Z. Demircioğlu, Ç.A. Kaştaş, O. Büyükgüngör, “Theoretical analysis (NBO, NPA, Mulliken Population Method) and molecular orbital studies (hardness, chemical potential, electrophilicity and Fukui function analysis) of (*E*)-2-((4-hydroxy-2-methylphenylimino)methyl)-3-methoxyphenol”, *J. Mol. Struct.*, **1091** (2015) 183–195.
- [82] P. Lu, Y. Wu, H. Kang, H. Wei, H. Liu, M. Fang, “What can pK_a and NBO charges of the ligands tell us about the water and thermal stability of metal organic frameworks?”, *J. Mater. Chem. A*, **2** (2014) 16250–16267.
- [83] A. Thirunavukkarasu, R. Karunathan, J. Mallika, V. Sathyanarayananamoorthi, “Vibrational and quantum chemical analysis of 3-methyl-2,6-diphenyl piperidin-4-one using HF and DFT methods”, *Indian J. Pure Appl. Phys.*, **52** (2014) 653–670.
- [84] F.S. Tiago, P.H.O. Santiago, M.M.P. Amaral, J.B.L. Martins, C.C. Gatto, “New Cu(II) complex with acetylpyridine benzoyl hydrazone: experimental and theoretical analysis”, *J. Coord. Chem.*, **69** (2016) 330–342.
- [85] N. Günay, Ö. Tamer, D. Kuzalic, D. Avc, Y. Atalay, “Theoretical investigation of *N*-methyl-*N'*-(4-nitrobenzylidene) pyrazine-2-carbohydrazide: Conformational study, NBO analysis, molecular structure and NMR spectra”, *Acta Phys. Pol. A*, **127** (2015) 701–710.

- [86] P.S. Kushwaha, P.C. Mishra, “Molecular electrostatic potential maps of the anti-cancer drugs daunomycin and adriamycin: an *ab initio* theoretical study”, *J. Mol. Struct. (Theochem)*, **636** (2003) 149–156.
- [87] S. Gatfaoui, N. Issaoui, A. Mezni, F. Bardak, T. Roisnel, A. Atac, H. Marouani, “Synthesis, structural and spectroscopic features, and investigation of bioactive nature of a novel organic-inorganic hybrid material 1*H*-1,2,4-triazole-4-ium trioxonitrate”, *J. Mol. Struct.*, **1150** (2017) 242–257.
- [88] N. Kalaiarasi, S. Manivarman, “Synthesis, spectroscopic characterization, computational exploration of 6-(2-(2,4-dinitrophenylhydrazano)-tetrahydro-2-thioxopyrimidin-4(1*h*)-one”, *Orient. J. Chem.*, **33** (2017) 304–317.
- [89] S.E. Kariper, K. Sayin, D. Karakas, “Theoretical study on the antitumor properties of Ru(II) complexes containing 2-pyridyl, 2-pyridine-4-carboxylic acid ligands”, *J. Mol. Struct.*, **1149** (2017) 473–486.
- [90] A. Kumer, N. Sarker, S. Paul, “The simulating study of *HOMO*, *LUMO*, thermo physical and quantitative structure of activity relationship (QSAR) of some anticancer active ionic liquids”, *EJERE*, **3** (2019) 1–10.
- [91] J.L. Gázquez, A. Cedillo, A. Vela, “Electrodonating and electroaccepting powers”, *J. Phys. Chem. A*, **111** (2007) 1966–1970.
- [92] J. Frau, D. Glossman-Mitnik, “Conceptual DFT descriptors of amino acids with potential corrosion inhibition properties calculated with the latest Minnesota Density Functionals”, *Front. Chem.*, **5** (2017) 1–8.
- [93] J. Frau, D. Glossman-Mitnik, “Conceptual DFT study of the local chemical reactivity of the colored BISARG melanoidin and its protonated derivative”, *Front. Chem.*, **6** (2018) 1–9.
- [94] N. Flores-Holguín, J. Frau, D. Glossman-Mitnik, “Conceptual DFT as a chemoinformatics tool for the study of the Taltobulin anticancer peptide”, *BMC Res. Notes*, **12** (2019) 1–4.
- [95] P.K. Chattaraj, A. Chakraborty, S. Giri, “Net Electrophilicity”, *J. Phys. Chem. A*, **113** (2009) 10068–10074.
- [96] U. Banik, S. Parasuraman, A.K. Adhikary, N.H. Othman, “Curcumin: the spicy modulator of breast carcinogenesis”, *J. Exp. Clin. Cancer Res.*, **36** (2017) 1–16.
- [97] W. Chanput, J.J. Mes, H.J. Wichers, “THP-1 cell line: An *in vitro* cell model for immune modulation approach”, *Int. Immunopharmacol.*, **23** (2014) 37–45.
- [98] H. Bosshart, M. Heinzelmann, “THP-1 cells as a model for human monocytes”, *Ann. Transl. Med.*, **4** (2016) 1–4.

Table 1: Crystal and structure refinement data for Hdmp and 1–6.

Compound	Hdmp	1	2	3
Formula	$C_{12}H_{15}NO_3$	$C_{31}H_{36}CeN_3O_{11}$, $2(CH_4O)$	$C_{31}H_{36}NdN_3O_{11}$, $2(CH_4O)$	$C_{64}H_{76}Gd_2N_6O_{22}$, $6(CH_4O)$
M_r (g.mol ⁻¹)	221.25	830.83	834.95	1788.05
Crystal system	Orthorhombic	Monoclinic	Monoclinic	Triclinic
Space group	<i>Pbca</i> (No. 61)	<i>I2/a</i> (No. 15)	<i>I2/a</i> (No. 15)	<i>P-1</i> (No. 2)
a, b, c [Å]	8.8959(4), 8.0239(3), 32.9010(14)	22.8156(9), 12.5043(5), 27.7448(11)	22.7183(18), 12.4573(11), 27.852(2)	11.7874(5), 17.7660(8), 21.0024(10)
α, β, γ (°)	90, 90, 90	90, 93.288(3), 90	90, 92.929(6), 90	73.394(2), 78.014(2), 80.235(2)
V (Å ³)	2348.47(17)	7902.4(5)	7872.1(11)	4094.3(3)
Z	8	8	8	2
ρ (g cm ⁻³)	1.252	1.397	1.409	1.450
μ (mm ⁻¹)	0.090	1.214	1.381	1.685
$F(000)$	944	3400	3416	1828
Crystal size (mm)	0.17 × 0.24 × 0.61	0.09 × 0.16 × 0.37	0.18 × 0.39 × 0.69	0.06 × 0.30 × 0.50
θ (min-max) (°)	2.5, 28.3	1.8, 28.3	2.3, 28.4	1.2, 28.4
Data set	$-11 \leq h \leq 11$; $-10 \leq k \leq 10$; $-43 \leq l \leq 43$	$-30 \leq h \leq 26$; $-16 \leq k \leq 16$; $-36 \leq l \leq 37$	$-29 \leq h \leq 30$; $-16 \leq k \leq 16$; $-37 \leq l \leq 37$	$-15 \leq h \leq 15$; $-23 \leq k \leq 23$; $-27 \leq l \leq 28$
Tot., Unique data, R_{int}	62507, 2927, 0.025	90084, 9810, 0.025	55211, 9815, 0.018	92833, 20449, 0.030
Observed [$I > 2\sigma(I)$] reflections	2530	8693	8839	16558
$N_{reflections}, N_{parameters}$	2927, 152	9810, 486	9815, 486	20449, 1023
$R[F^2 > 2\sigma(F^2)]$, $wR(F^2)$, S	0.0499, 0.1309, 1.12	0.0186, 0.0456, 1.06	0.0241, 0.0726, 1.14	0.0282, 0.0650, 1.08
$\Delta\rho_{min}, \Delta\rho_{max}$ (e.Å ⁻³)	-0.19, 0.31	-0.47, 0.83	-0.85, 1.49	-0.93, 2.10

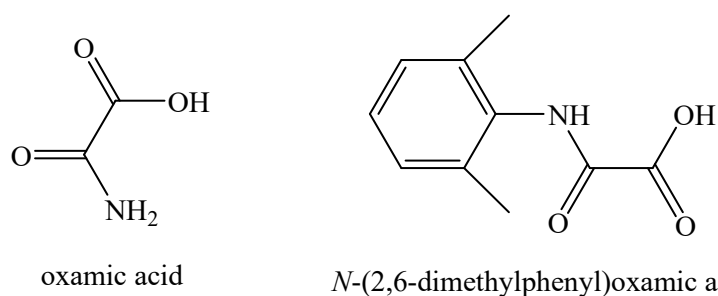
Compound	4	5	6
Formula	$C_{61}H_{70}Er_2N_6O_{22}$, $2(CH_4O)$	$C_{82}H_{95.54}N_8Na_2Nd_2O_{30.46}$, C_2H_6O, O	$C_{81.41}H_{94.22}Gd_2N_8Na_2O_{30.30}$, C_2H_6O, O
M_r (g.mol ⁻¹)	1637.83	2077.02	2092.04
Crystal system	Triclinic	Triclinic	Triclinic
Space group	<i>P-1</i> (No. 2)	<i>P-1</i> (No. 2)	<i>P-1</i> (No. 2)
a, b, c [Å]	14.5404(7), 14.9104(7), 19.1140(9)	11.4098(6), 20.9380(11), 21.5456(11)	11.3308(5), 20.7995(10), 21.5254(10)
α, β, γ (°)	106.487(2), 95.985(2), 116.654(2)	111.678(2), 93.897(3), 99.470(3)	111.771(2), 93.982(2), 98.973(2)
V (Å ³)	3419.2(3)	4671.2(4)	4608.5(4)
Z	2	2	2
ρ (g cm ⁻³)	1.591	1.477	1.508
μ (mm ⁻¹)	2.519	1.193	1.522
$F(000)$	1652	2126	2130
Crystal size (mm)	0.11 × 0.41 × 0.70	0.11 × 0.25 × 0.32	0.26 × 0.36 × 0.64
θ (min-max) (°)	1.6, 28.4	1.7, 28.3	1.8, 28.4
Data set	$-19 \leq h \leq 18$; $-13 \leq k \leq 19$; $-25 \leq l \leq 25$	$-15 \leq h \leq 15$; $-27 \leq k \leq 27$; $-28 \leq l \leq 28$	$-15 \leq h \leq 15$; $-27 \leq k \leq 27$; $-28 \leq l \leq 28$
Tot., Unique data, R_{int}	61425, 17016, 0.018	168732, 23318, 0.039	328132, 22936, 0.022
Observed [$I > 2\sigma(I)$] reflections	15123	18870	20375
$N_{reflections}, N_{parameters}$	17016, 924	23318, 1221	22936, 1227
$R[F^2 > 2\sigma(F^2)]$, $wR(F^2)$, S	0.0204, 0.0472, 1.15	0.0292, 0.0740, 1.03	0.0242, 0.0626, 1.14

$\Delta\rho_{\min}, \Delta\rho_{\max} (\text{e} \cdot \text{\AA}^{-3})$

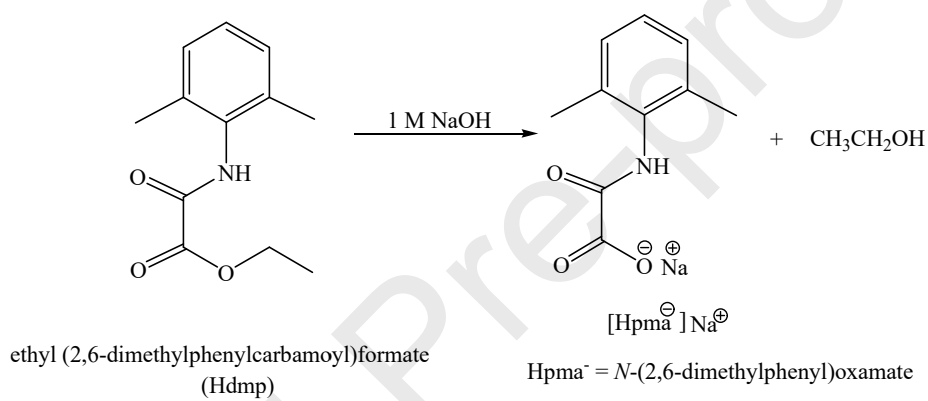
-0.94, 1.58

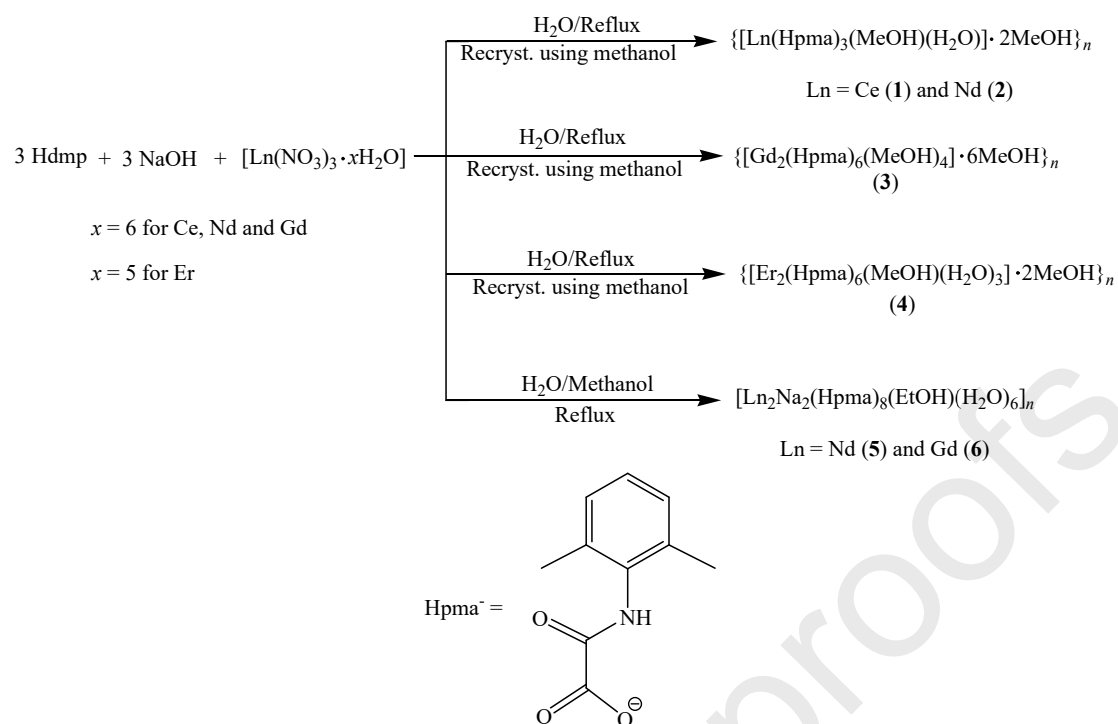
-0.99, 1.18

-1.79, 1.35



oxamic acid

N-(2,6-dimethylphenyl)oxamic acid**Figure 1:** Structures of oxamic acid and *N*-(2,6-dimethylphenyl)oxamic acid [9-11].ethyl (2,6-dimethylphenylcarbamoyl)formate
(Hdmp)[Hpma⁻]Na⁺
Hpma⁻ = *N*-(2,6-dimethylphenyl)oxamate**Scheme 1:** Hydrolysis of the proligand Hdmp to the anionic oxamate ligand Hpma⁻.



Scheme 2: Schematic diagram for the preparation of the six metal complexes derived from Hdmp.

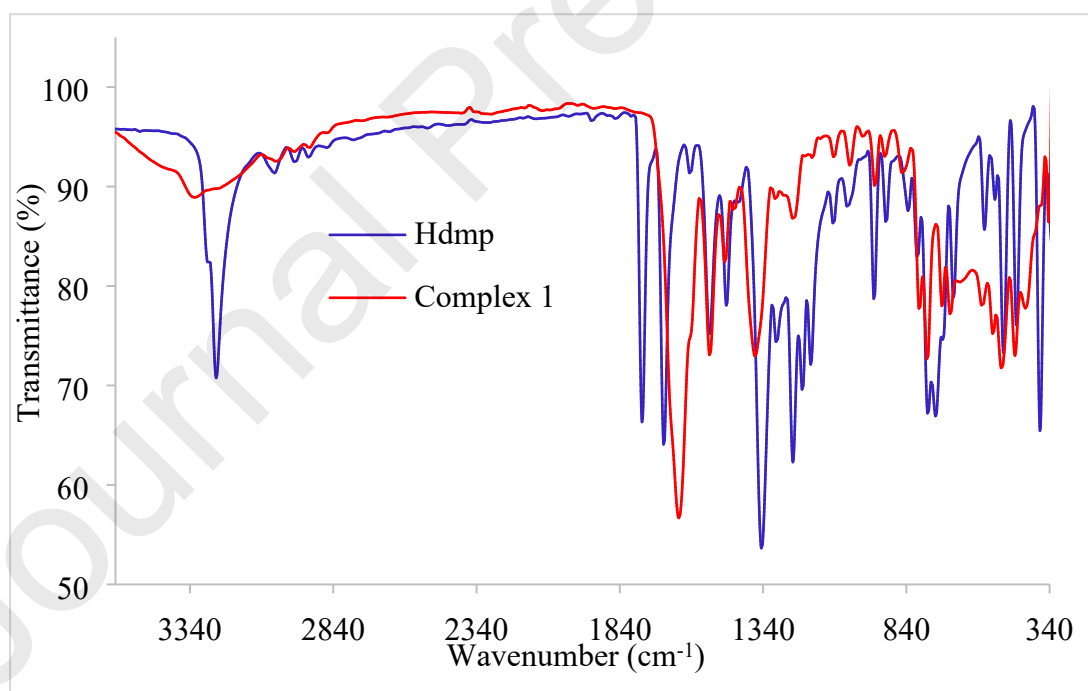


Figure 2: Overlay IR spectra of Hdmp and complex 1.

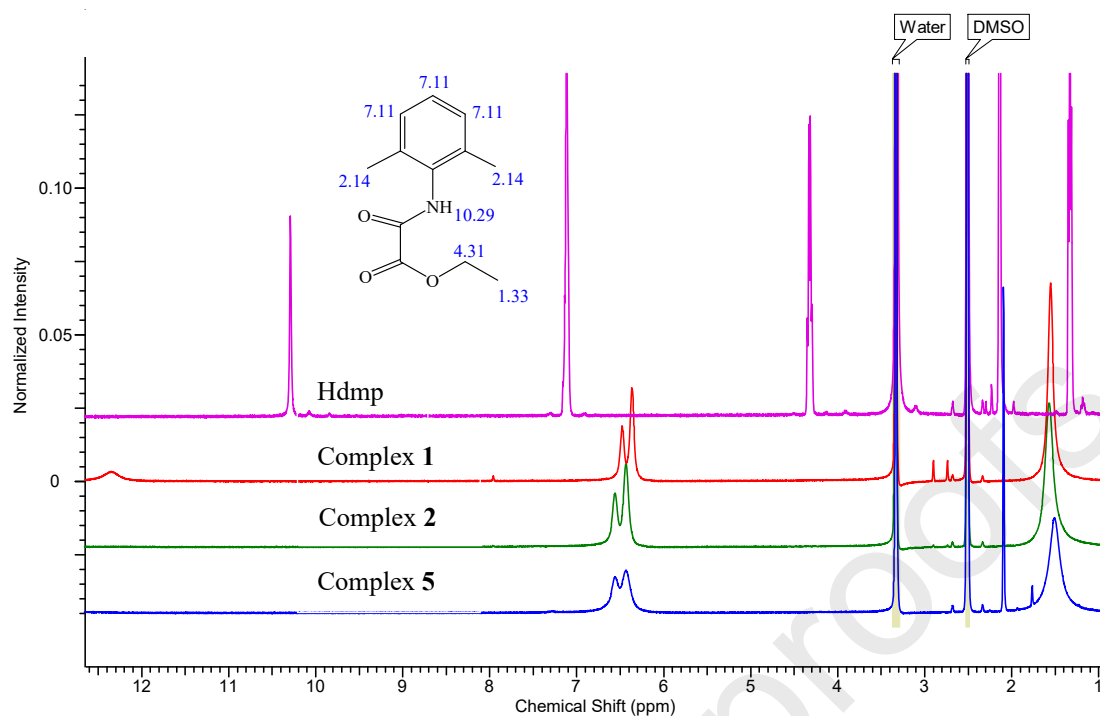


Figure 3: Overlay ^1H NMR spectra of Hdmp, and the Ln(III) complexes 1, 2 and 5 in $\text{DMSO}-d_6$.

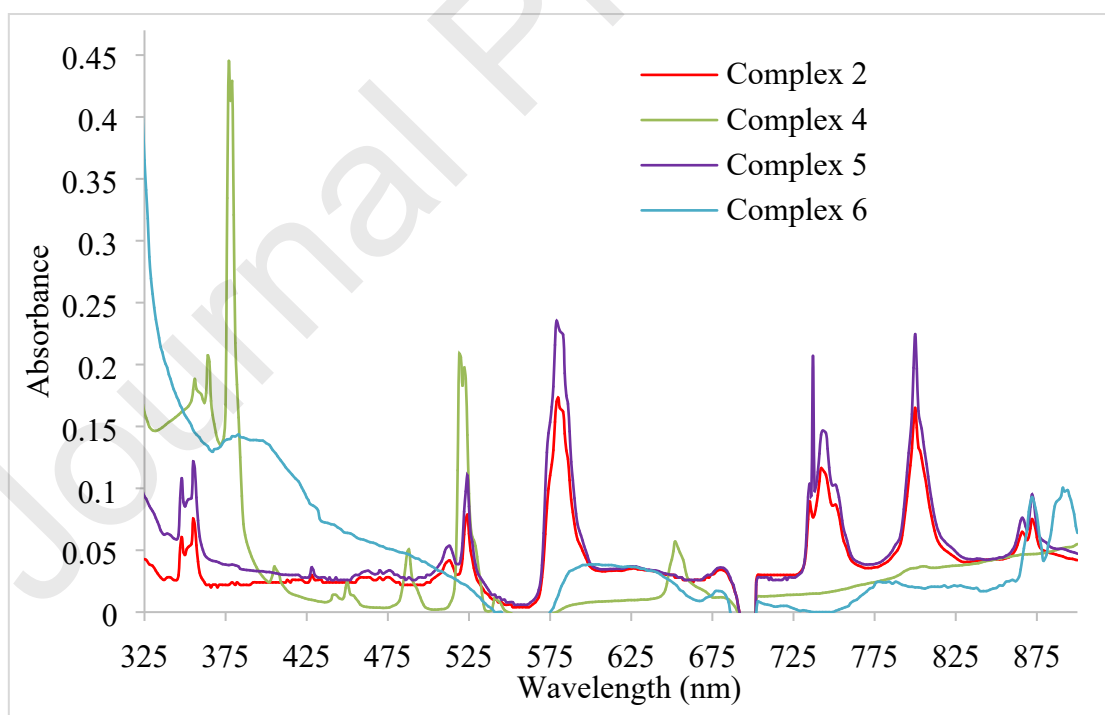


Figure 4: The UV-Vis-NIR spectra of 2, 4, 5 and 6 in DMF.

Table 2: Absorption bands for complexes **2** and **4–6** [26-29,31-35].

Complex 2 and 5		Complex 4	
λ_{\max} (nm)	<i>J</i> -levels	λ_{\max} (nm)	<i>J</i> -levels
348, 356	$^4I_{9/2} \rightarrow ^4D_{3/2} + ^4D_{5/2}$ $+ ^4D_{1/2} + ^2I_{11/2}$	360	$^4I_{15/2} \rightarrow ^2G_{7/2}$
432	$\rightarrow ^2P_{1/2}$	365	$\rightarrow (^4G_{9/2}, ^2K_{15/2})$
511	$\rightarrow ^4G_{9/2}$	379	$\rightarrow ^4G_{11/2}$
522	$\rightarrow ^4G_{7/2}$	409	$\rightarrow ^2H_{9/2}$
582	$\rightarrow ^4G_{5/2} + ^2G_{7/2}$	446	$\rightarrow ^4F_{5/2}$
745	$\rightarrow ^4F_{7/2} + ^4S_{3/2}$	452	$\rightarrow ^4F_{3/2}$
800	$\rightarrow ^4F_{5/2} + ^2H_{9/2}$	491	$\rightarrow ^4F_{7/2}$
869, 876	$\rightarrow ^4F_{3/2}$	522	$\rightarrow ^2H_{11/2}$
		544	$\rightarrow ^4S_{3/2}$
		654	$\rightarrow ^4F_{9/2}$
Complex 6			
~381	$^8S_{7/2} \rightarrow ^6P_{7/2}$		

Table 3: Summary of *SHAPE* analysis for complexes **1–6**.

Complex	Coordination number	Shape (and symmetry)	CShM	Polyhedral volume (Å ³)	Average bond length (Å)
1	9	TCTPR-9 (<i>D</i> _{3h})	0.85318	32.4845	2.5247
2	9	TCTPR-9 (<i>D</i> _{3h})	0.77701	31.3620	2.4944
3	9 (Gd1)	CSAPR-9 (<i>C</i> _{4v})	0.46072	29.0919	2.4407
	9 (Gd2)	CSAPR-9 (<i>C</i> _{4v})	0.42825	29.1601	2.4417
4	8 (Er1)	SAPR-8 (<i>D</i> _{4d})	0.43454	22.5763	2.3547
	9 (Er2)	CSAPR-9 (<i>C</i> _{4v})	0.28116	27.2691	2.3890
5	9 (Nd1)	CSAPR-9 (<i>C</i> _{4v})	0.87740	30.5853	2.4865
	9 (Nd2)	CSAPR-9 (<i>C</i> _{4v})	0.94332	30.5194	2.4904
	6 (Na1)	OC-6 (<i>O</i> _h)	1.90099	18.0288	2.4206
	5 (Na2)	vOC-5 (<i>C</i> _{4v})	3.09930	10.9901	2.4329
6	9 (Gd1)	CSAPR-9 (<i>C</i> _{4v})	0.68425	29.0390	2.4405
	9 (Gd2)	CSAPR-9 (<i>C</i> _{4v})	0.76846	28.9252	2.4428
	6 (Na1)	OC-6 (<i>O</i> _h)	2.08861	17.7130	2.4086
	5 (Na2)	vOC-5 (<i>C</i> _{4v})	3.00016	10.8749	2.4208

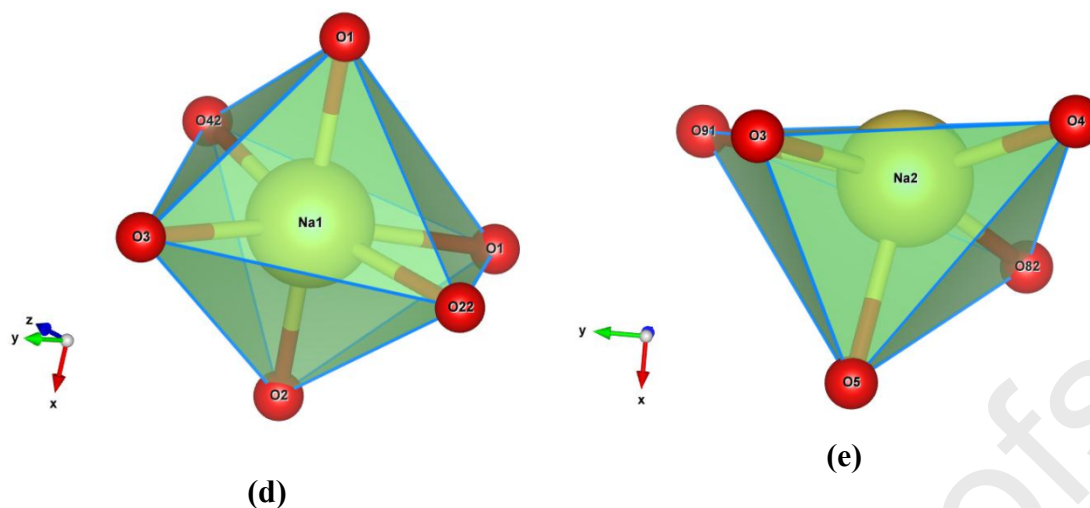


Figure 5: The polyhedral views showing the geometries of the coordination environments of: (a) the Ce(III) ion in **1**; (b and c) the eight- and nine-coordinate Er(III) ions in **4**; (d and e) the six- and five-coordinate Na(I) ions in **5**.

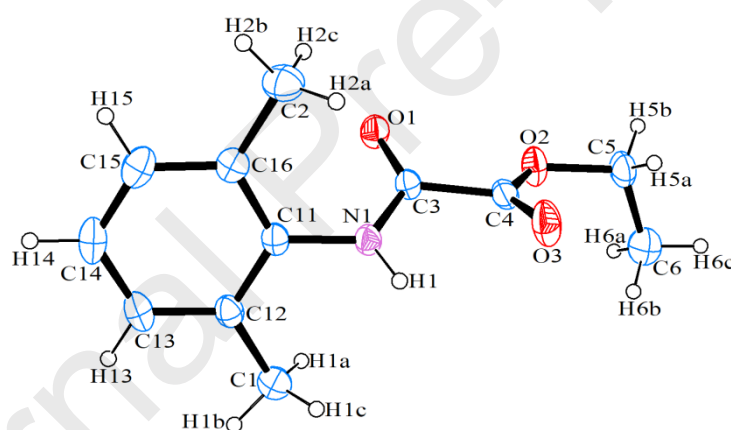


Figure 6a: ORTEP view of the proligand Hdmp showing 50% probability displacement ellipsoids and atom-labelling.

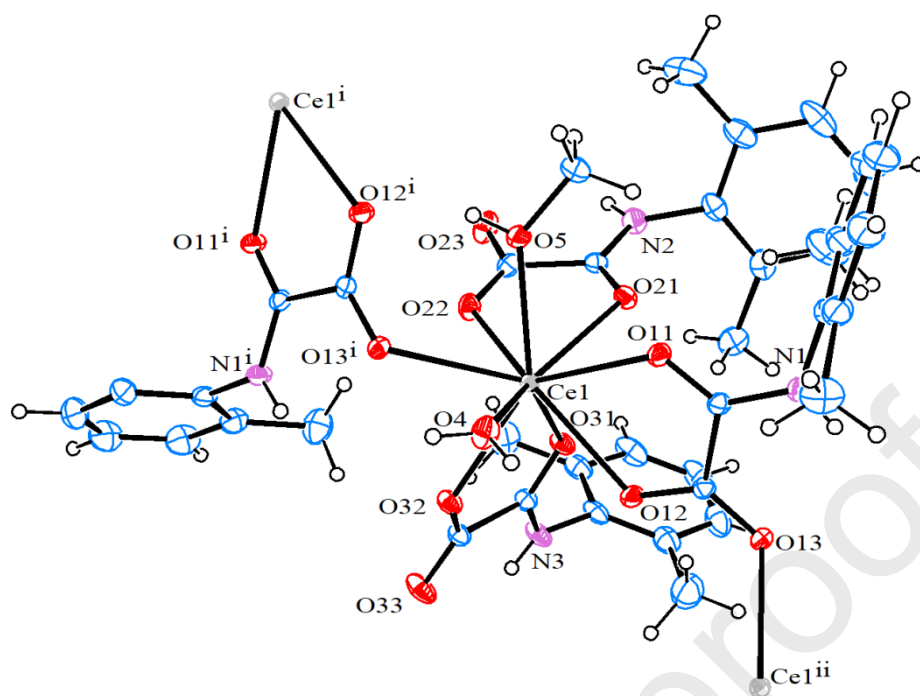


Figure 6b: The structure of the molecule present in complex 1 (30% probability ellipsoids).
Complex 2 exhibits a similar coordination environment.

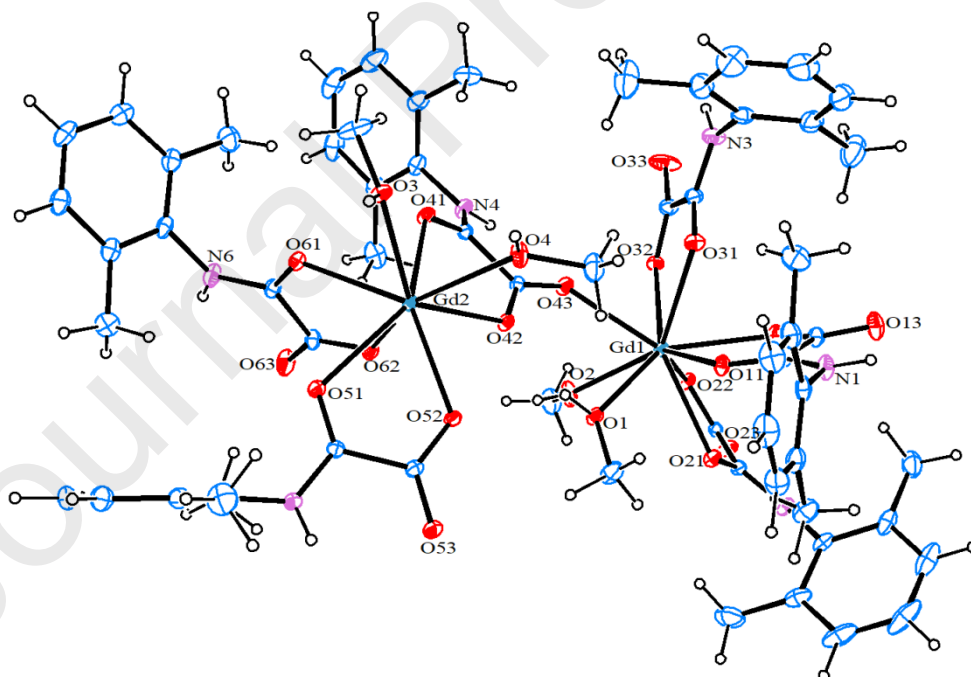


Figure 6c: Molecular structure of the dinuclear unit of 3 with displacement ellipsoids drawn at the 30% probability level.

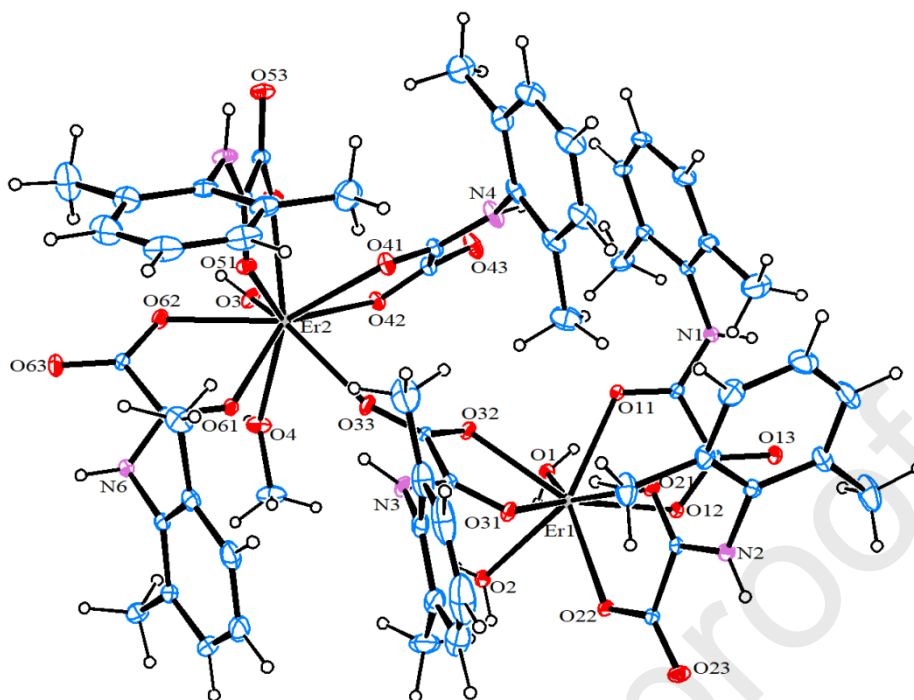


Figure 6d: ORTEP view of the dinuclear unit of **4** showing 30% probability displacement ellipsoids and the partial atom-labelling scheme.

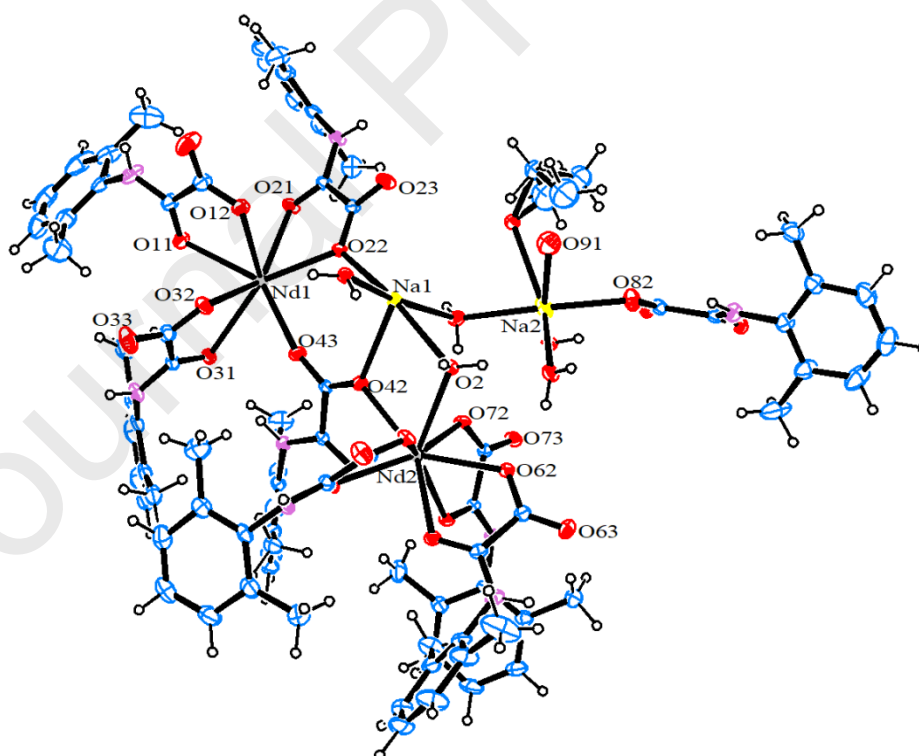


Figure 6e: ORTEP diagram (thermal ellipsoids at 30% probability) with a partial atom-numbering scheme for the heterometallic complex found in **5** (complex **6** has a similar structure to that of complex **5**).

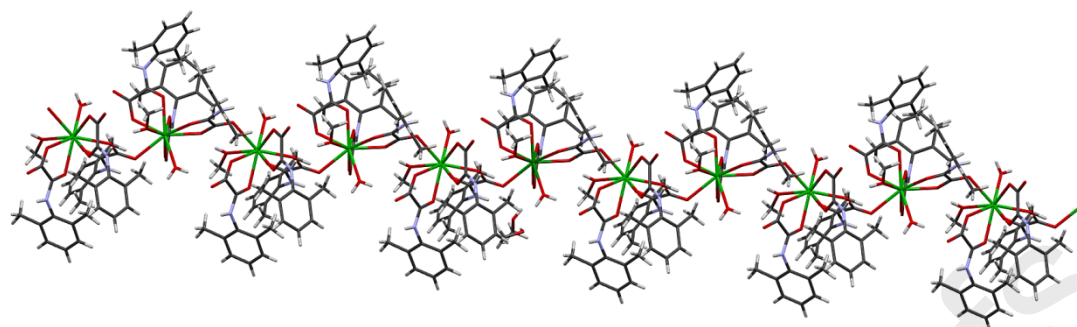


Figure 6f: One-dimensional zig-zag network in **1** constructed by μ_2 -Hpma⁻ (Key: Ln = green, C = grey, N = blue, O = red).

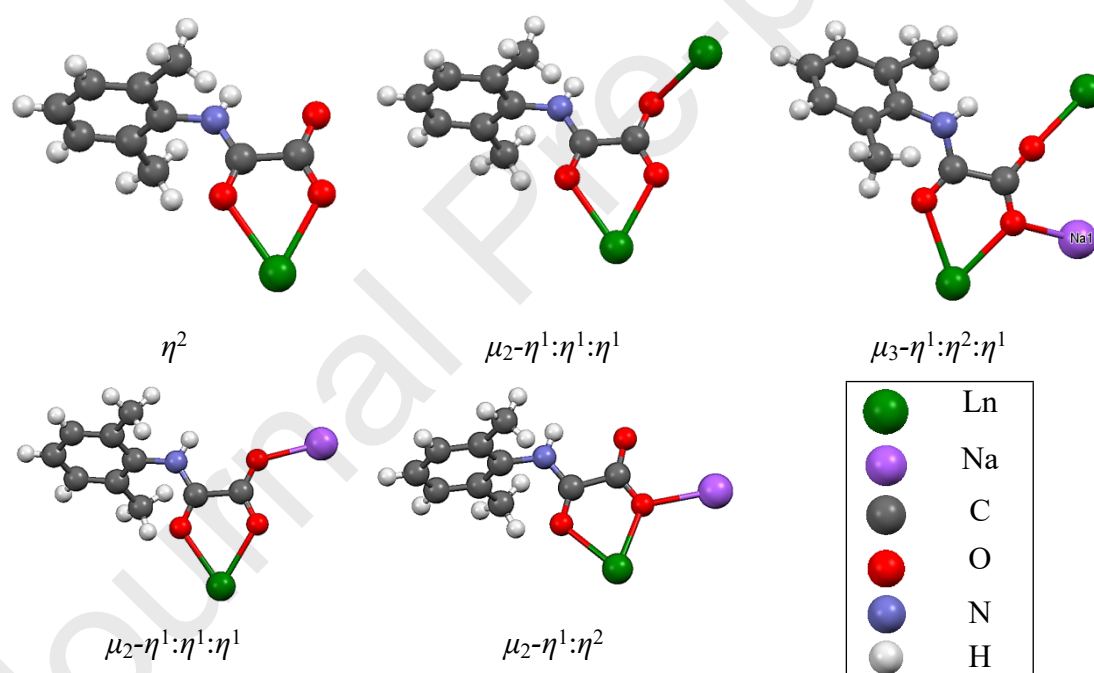


Figure 6g: The coordination modes of Hpma⁻ in the metal complexes (binding modes containing Na(I) ions belong to **5** and **6** only) [48-50].

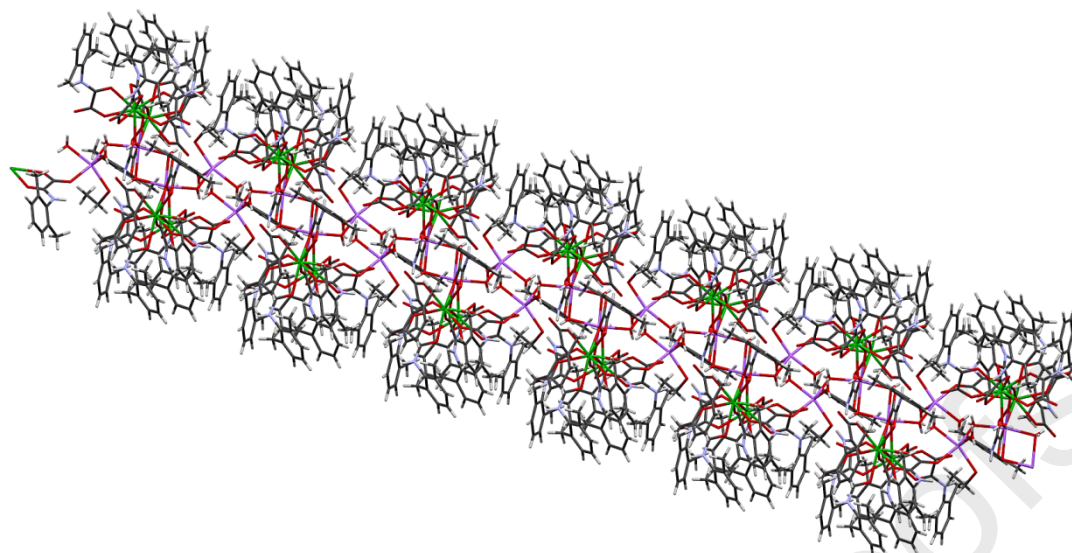


Figure 6h: 1D network in **5** and **6** linked via μ_2 -Hpma⁻, μ_3 -Hpma⁻, as well as μ_2 -H₂O (Key: Ln = green, Na = purple, C = grey, N = blue, O = red).

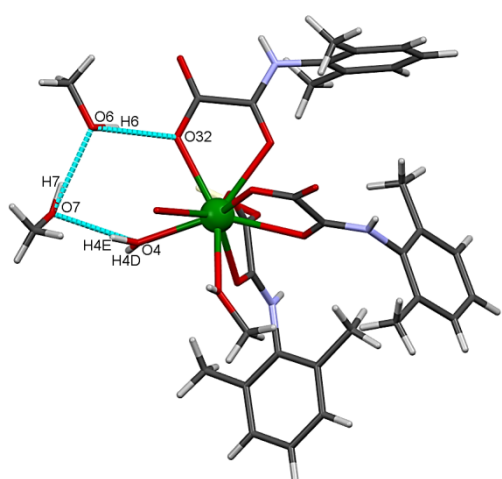
Table 4a: Selected geometric parameters (Å, °) for Hdmp and lanthanide complexes **1–3**.

Hdmp	{[Ln(Hpma) ₃ (MeOH)(H ₂ O)]·2MeOH} _n		{[Gd ₂ (Hpma) ₆ (MeOH) ₄]·6MeOH} _n			
	1 (Ln = Ce)	2 (Ln = Nd)	3			
Bond lengths (Å)						
O1-C3	1.2140(17)	Ln1-O4	2.5049(13)	2.471(2)	Gd1-O1	2.459(2)
O2-C4	1.3138(17)	Ln1-O5	2.5404(12)	2.5065(17)	Gd1-O2	2.478(2)
O2-C5	1.4651(19)	Ln1-O11	2.5296(12)	2.4978(16)	Gd1-O11	2.3901(19)
O3-C4	1.1914(19)	Ln1-O12	2.5190(10)	2.4943(17)	Gd1-O12	2.4376(19)
N1-C3	1.3384(17)	Ln 1-O21	2.5457(12)	2.5163(18)	Gd1-O21	2.5087(19)
N1-C11	1.4286(17)	Ln1-O22	2.4752(12)	2.4426(17)	Gd1-O22	2.3782(18)
C1-C12	1.502(2)	Ln1-O31	2.5684(12)	2.5339(17)	Gd1-O31	2.4824(19)
N1-H1	0.846(16)	Ln1-O32	2.4926(12)	2.4603(17)	Gd1-O32	2.4010(18)
		Ln1-O13a	2.5469(11)	2.5253(16)	Gd1-O43	2.4320(19)
		Ln··Ln	6.289	6.271	Gd··Gd	6.294
Bond angles (°)						
C4-O2-C5	116.99(12)	O11-Ln1-O12	63.51(4)	63.99(5)	O11-Gd1-O12	67.24(6)
C3-N1-C11	122.93(12)	O21-Ln1-O22	65.11(4)	65.92(5)	O21-Gd1-O22	66.10(6)
C3-N1-H1	115.8(11)	O31-Ln1-O32	63.52(4)	64.37(5)	O31-Gd1-O32	66.13(6)
O1-C3-N1	125.49(13)				O41-Gd2-O42	66.52(6)
N1-C3-C4	112.58(12)				O51-Gd2-O52	66.68(6)
O2-C4-O3	126.63(14)				O61-Gd2-O62	66.49(6)

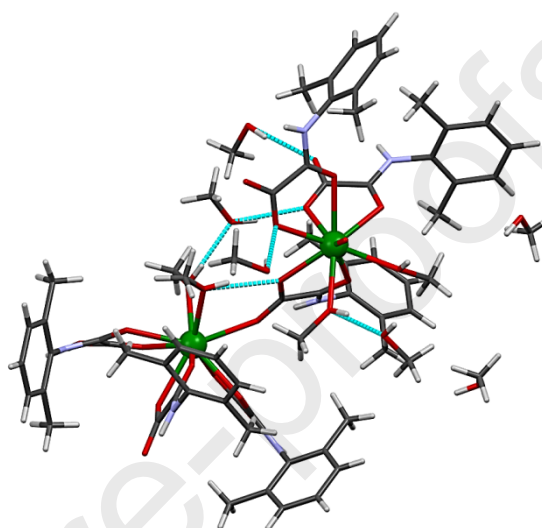
Table 4b: Selected bond lengths (Å) and angles (°) for metal complexes 4–6.

$\{\{\text{Er}_2(\text{Hpma})_6(\text{MeOH})(\text{H}_2\text{O})_3\} \cdot 2\text{MeOH}\}_n$		$[\text{Ln}_2\text{Na}_2(\text{Hpma})_8(\text{EtOH})(\text{H}_2\text{O})_6]_n$		
4		5 (Ln = Nd)		6 (Ln = Gd)
Bond lengths (Å)		Bond lengths (Å)		
Er1-O1	2.3537(17)	Ln1-O11	2.496(2)	2.449(2)
Er1-O2	2.3369(19)	Ln1-O12	2.493(2)	2.4522(18)
Er1-O11	2.3240(18)	Ln1-O21	2.4747(18)	2.4296(17)
Er1-O12	2.3547(18)	Ln1-O22	2.4622(17)	2.4134(16)
Er1-O21	2.4051(15)	Ln1-O31	2.5465(16)	2.5012(14)
Er1-O22	2.2722(18)	Ln1-O32	2.5002(19)	2.4469(17)
Er1-O31	2.4227(18)	Ln1-O43	2.430(2)	2.3930(18)
Er1-O32	2.3681(18)	Ln1-O81b	2.4765(19)	2.4359(17)
Er2-O33	2.3333(18)	Ln1-O83b	2.4945(19)	2.4404(17)
Er...Er	6.497	Na1-O1	2.327(2)	2.311(2)
		Na1-O2	2.566(2)	2.544(2)
		Na1-O3	2.388(2)	2.3845(19)
Bond angles (°)		Na1-O22	2.476(2)	2.461(2)
O11-Er1-O12	69.75(6)	Na1-O42	2.3865(19)	2.3771(16)
O21-Er1-O22	69.80(6)	Na1-O1a	2.383(2)	2.3760(18)
O31-Er1-O32	67.12(6)	Ln...Ln	6.843	6.768
O41-Er2-O42	66.97(5)	Na...Na	4.171	4.169
O51-Er2-O52	67.58(6)			
O61-Er2-O62	67.72(6)			
		Bond angles (°)		
		O11-Ln1-O12	64.96(7)	65.94(6)
		O21-Ln1-O22	66.29(6)	67.52(6)
		O22-Ln1-O43	76.01(6)	75.19(6)

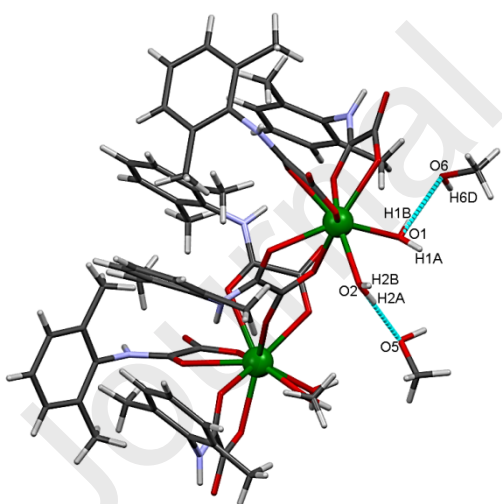
O31-Ln1-O32	64.08(6)	65.27(5)
O41-Ln2-O42	64.35(6)	65.50(5)
O52-Ln2-O53	65.41(6)	66.58(5)
O61-Ln2-O62	66.09(6)	67.28(6)
O71-Ln2-O72	65.55(5)	66.68(5)



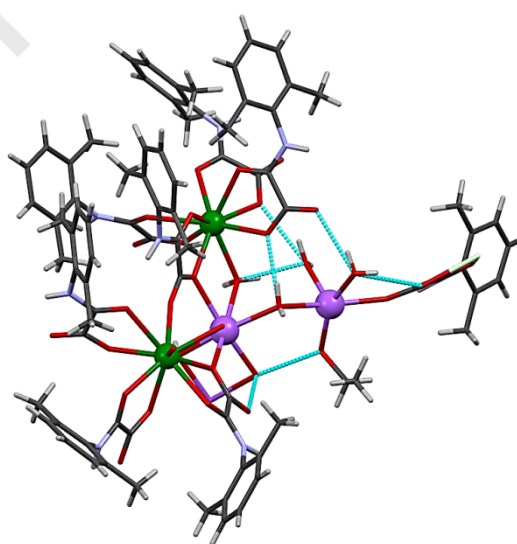
Complex 1



Complex 3



Complex 4



Complexes 5 and 6

Figure 6i: Hydrogen bonding interactions in metal complexes 1 and 3–6.

Table 4c: Selected hydrogen bonding geometries (Å, °) for Hdmp and 1–4.

Hdmp				
<i>D-H...A</i>	<i>D-H</i>	<i>H...A</i>	<i>D...A</i>	<i>D-H...A</i>
N1-H1...O3	0.846(16)	2.408(17)	2.7389(17)	104.0(13)
N1-H1...O1 ⁱ	0.846(16)	2.232(17)	3.0519(16)	163.3(16)
C1-H1C...O1 ⁱ	0.9600	2.5900	3.448(2)	149.00
C2-H2C...O1	0.9600	2.5000	3.083(2)	119.00
Complex 1				
<i>D-H...A</i>	<i>D-H</i>	<i>H...A</i>	<i>D...A</i>	<i>D-H...A</i>
N1-H1...O13	0.84(2)	2.35(2)	2.7156(17)	106.7(16)
N1-H1...O6 ⁱ	0.84(2)	2.13(2)	2.9335(18)	160.6(18)
N2-H2...O23	0.80(2)	2.23(2)	2.6601(19)	114.4(17)
N3-H3...O33 ⁱⁱ	0.81(2)	2.05(2)	2.8154(18)	156.5(19)
O4-H4D...O23 ⁱ	0.831(16)	1.936(16)	2.7506(17)	166(2)
O4-H4E...O7	0.839(16)	2.000(17)	2.825(2)	168(2)
O5-H5...O12	0.832(14)	1.934(18)	2.7157(16)	156.2(19)
Complex 2				
<i>D-H...A</i>	<i>D-H</i>	<i>H...A</i>	<i>D...A</i>	<i>D-H...A</i>
N1-H1...O13	0.86(4)	2.32(3)	2.719(3)	109(3)
N1-H1...O6 ⁱ	0.86(3)	2.12(4)	2.934(3)	157(3)
N2-H2...O23	0.86(4)	2.24(3)	2.657(3)	110(3)
N3-H3...O33	0.77(3)	2.43(3)	2.727(3)	105(3)
O4-H4D...O23 ⁱ	0.83(2)	1.95(2)	2.761(3)	164(3)
O4-H4E...O7	0.856(19)	2.00(2)	2.843(4)	169(3)
O6-H6...O32	0.8400	1.8700	2.692(3)	164.00
Complex 3				
<i>D-H...A</i>	<i>D-H</i>	<i>H...A</i>	<i>D...A</i>	<i>D-H...A</i>
N1-H1...O9 ⁱ	0.89(3)	2.10(3)	2.845(4)	141(3)
N1-H1...O13	0.89(3)	2.33(4)	2.692(3)	104(3)
O1-H1D...O42	0.83(3)	1.90(3)	2.694(3)	159(3)
N2-H2...O7 ⁱ	0.88(2)	1.98(2)	2.821(3)	161(3)
O2-H2D...O6	0.81(4)	1.88(4)	2.681(3)	169(3)
O3-H3D...O22	0.84(3)	1.88(3)	2.685(3)	161(3)
N4-H4...O43	0.88(2)	2.39(3)	2.731(3)	103(2)
N4-H4...O70	0.88(2)	1.94(2)	2.802(3)	164(3)
O5-H5D...O63	0.8400	2.0000	2.796(3)	158.00
Complex 4				
<i>D-H...A</i>	<i>D-H</i>	<i>H...A</i>	<i>D...A</i>	<i>D-H...A</i>
N1-H1...O13	0.89(3)	2.37(3)	2.720(3)	104(2)
N1-H1...O63 ⁱ	0.89(3)	1.99(3)	2.825(3)	155(3)
O1-H1A...O23 ⁱⁱ	0.84(2)	1.81(2)	2.649(2)	175(4)
O2-H2A...O5	0.83(2)	1.83(2)	2.663(3)	175(2)
O2-H2B...O12 ⁱⁱ	0.84(4)	2.12(4)	2.954(3)	175(4)
O3-H3A...O1 ⁱⁱⁱ	0.80(4)	1.96(4)	2.755(3)	172(4)
O3-H3B...O42 ⁱⁱⁱ	0.78(4)	2.24(4)	2.929(2)	149(5)
O6-H6D...O63 ⁱⁱⁱ	0.8400	2.2600	3.012(3)	150.00

D = donor, A = acceptor. **Symmetry codes** for **Hdmp**: (i) $1/2-x, -1/2+y, z$. for **1**: (i) $1-x, 1/2+y, 1/2-z$; (ii) $1/2-x, 3/2-y, 1/2-z$. for **2**: (i) $1-x, 1/2+y, 1/2-z$. for **3**: (i) $1-x, -y, 1-z$. for **4**: (i) $-1+x, -1+y, z$; (ii) $1-x, 1-y, 1-z$; (iii) $1-x, 2-y, 1-z$.

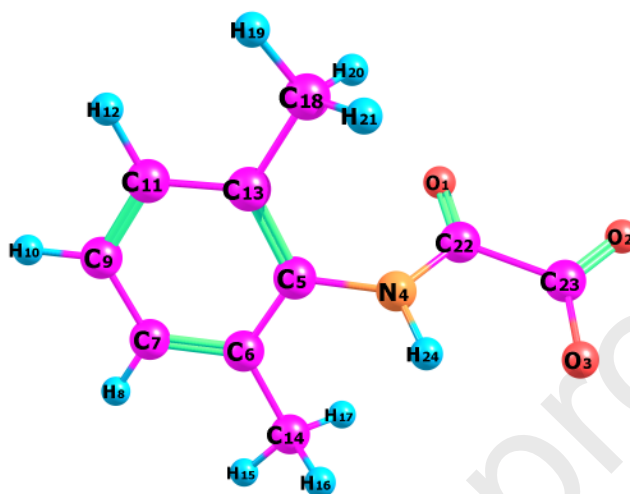


Figure 7a: Optimised B3LYP/aug-cc-pVTZ molecular structure of Hpma⁻ in DMSO.

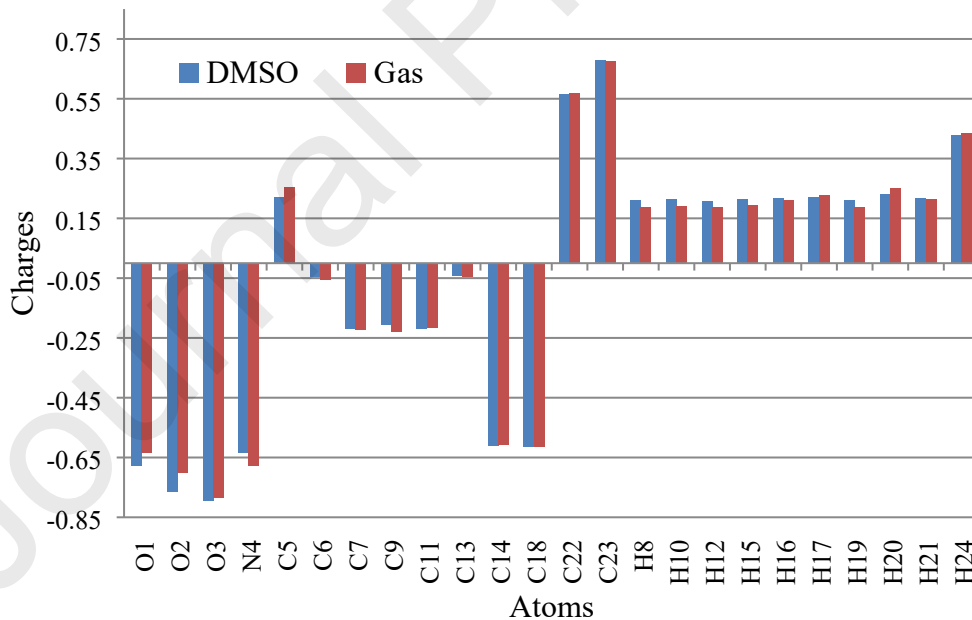


Figure 7b: The natural charge distribution of Hpma⁻ at DFT/B3LYP/aug-cc-pVTZ in the gas phase and DMSO.

Table 5: Accrual of natural charges in the core, valence and Rydberg orbitals for selected atoms of Hpma⁻ in DMSO.

Atom	Charge	Core	Valence	Rydberg	Total
O1	-0.67720	2.00000	6.65040	0.02680	8.67720
O2	-0.76420	2.00000	6.73769	0.02651	8.76420
O3	-0.79536	2.00000	6.76949	0.02588	8.79536
N4	-0.63544	1.99999	5.60139	0.03406	7.63544
C23	0.67881	1.99999	3.26991	0.05129	5.32119
C18	-0.61449	1.99999	4.60310	0.01140	6.61449
H12	0.20813	0.00000	0.78975	0.00213	0.79187
H24	0.42881	0.00000	0.56567	0.00553	0.57119

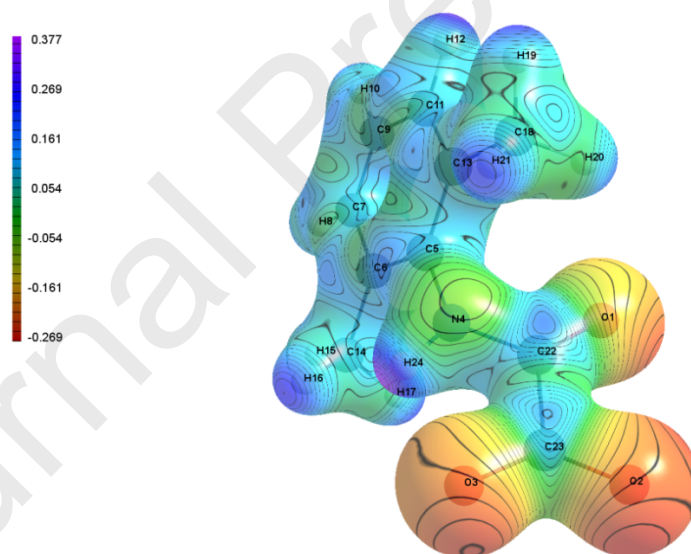


Figure 7c: The molecular electrostatic potential map of Hpma⁻ evaluated using the B3LYP/aug-cc-pVTZ method in DMSO.

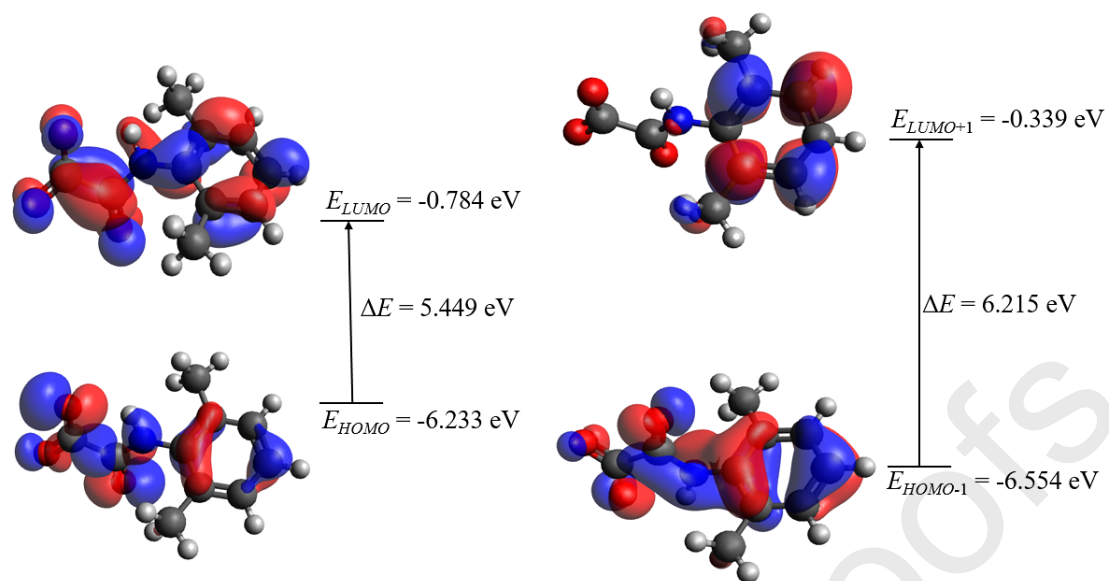


Figure 8: The frontier molecular orbitals plot of Hpma⁻ showing the *HOMO-LUMO* energy gaps for vicinal orbitals. An isovalue of 0.03 was used in creating the orbital surfaces.

Table 6: Global and chemical parameters of Hpma⁻ calculated with the B3LYP density functional with the aug-cc-pVTZ basis set and the SCRF-CPCM solvation model using DMSO as the solvent (softness in eV⁻¹ and other descriptors are in eV).

Global and chemical reactivity descriptor	Symbols	Values (eV)
Energy of <i>HOMO</i>	E_{HOMO}	-6.233
Energy of <i>LUMO</i>	E_{LUMO}	-0.784
Energy of <i>HOMO</i> -1	E_{HOMO-1}	-6.554
Energy of <i>LUMO</i> +1	E_{LUMO+1}	-0.339
Energy of <i>HOMO</i> -2	E_{HOMO-2}	-6.654
Energy of <i>LUMO</i> +2	E_{LUMO+2}	-0.245
First energy gap	$\Delta E = LUMO - HOMO$	5.449
Second energy gap	$\Delta E = LUMO+1 - HOMO-1$	6.215
Third energy gap	$\Delta E = LUMO+2 - HOMO-2$	6.409
Ionisation energy (I)	$-E_{HOMO}$	6.233
Electron affinity (A)	$-E_{LUMO}$	0.784
Hardness (η)	$\frac{(I-A)}{2}$	2.725
Chemical potential (μ)	$\frac{-(I+A)}{2}$	-3.509
Softness (σ)	$\frac{1}{\eta}$	0.367 eV⁻¹
Electrophilicity index (ω)	$\frac{\mu^2}{2\eta}$	2.259
Electronegativity (χ_m)	$\frac{I+A}{2}$	3.509
Electrodonating power (ω^-)	$\frac{(3I+A)^2}{16(I-A)}$	4.354
Electroaccepting power (ω^+)	$\frac{(I+3A)^2}{16(I-A)}$	0.845
Net electrophilicity ($\Delta\omega^\pm$)	$\omega^+ - (-\omega^-) = \omega^+ + \omega^-$	5.199

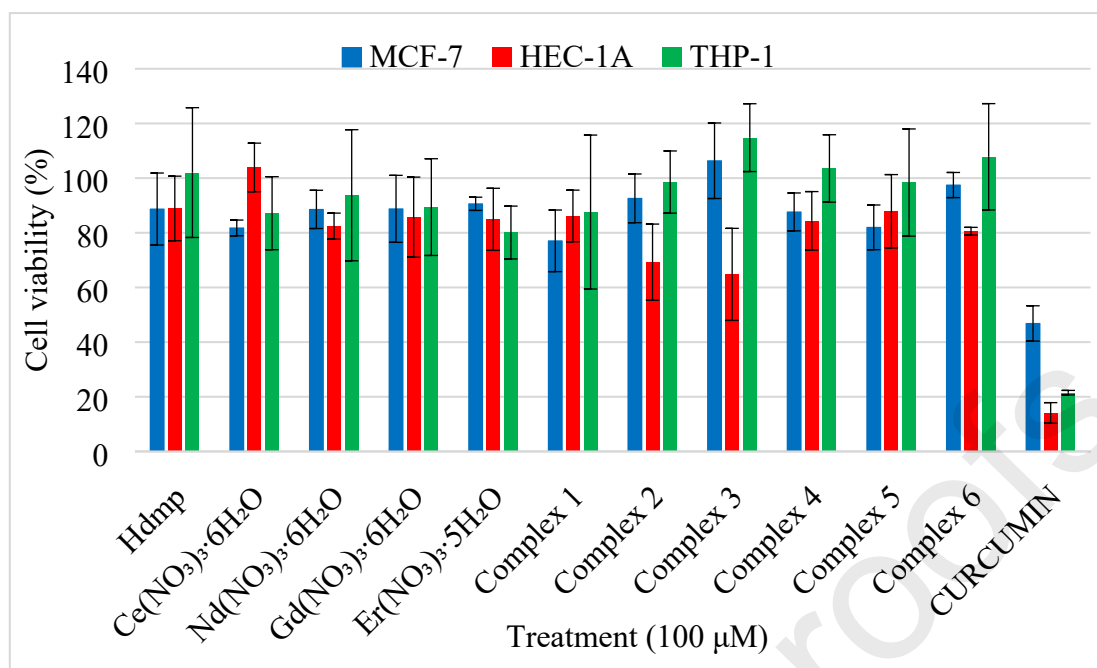


Figure 9: Cytotoxic effects of the compounds on MCF-7, HEC-1A and THP-1 cells using an MTT assay. Mean values of three independent experiments \pm SD are shown.

ABSTRACT

The complexation reactions of Ce(III), Nd(III), Gd(III) and Er(III) ions with the chelating/bridging monoanionic ligand *N*-(2,6-dimethylphenyl)oxamate (Hpma^-) in basic media were performed in view of the potential applications of oxamate derivatives as cytotoxic agents. The coordination compounds were characterised by different physico-chemical techniques: elemental analysis, conductivity measurements, IR, ^1H NMR and UV-Vis-NIR spectroscopy, and X-ray crystallography. The anionic Hpma^- ligand was obtained through conversion of the proligand ethyl (2,6-dimethylphenylcarbamoyl)formate (Hdmp). The reactions afforded lanthanide(III)–oxamate coordination polymers of the formulae: $\{[\text{Ln}(\text{Hpma})_3(\text{MeOH})(\text{H}_2\text{O})]\cdot 2\text{MeOH}\}_n$ ($\text{Ln} = \text{Ce}$ (1) and Nd (2)), $\{[\text{Gd}_2(\text{Hpma})_6(\text{MeOH})_4]\cdot 6\text{MeOH}\}_n$ (3), $\{[\text{Er}_2(\text{Hpma})_6(\text{MeOH})(\text{H}_2\text{O})_3]\cdot 2\text{MeOH}\}_n$ (4) and $[\text{Ln}_2\text{Na}_2(\text{Hpma})_8(\text{EtOH})(\text{H}_2\text{O})_6]_n$ ($\text{Ln} = \text{Nd}$ (5) and Gd (6)). The polymeric complexes feature Ln– Hpma moieties bridged by $\mu_2\text{-}\eta^1\text{:}\eta^1\text{:}\eta^1$ Hpma^- ligands, giving one-dimensional zig-zag chains of the –Ln–O–C–O–Ln– type. Atomic charge analysis and the MEP map of the Hpma^- moiety using the DFT/B3LYP method were consistent with the chelating and bridging modes of the anionic ligand through all the oxygen atoms. An evaluation of the cytotoxic activities of the metal salts, the proligand and the novel lanthanide complexes on MCF-7, HEC-1A and

THP-1 cells revealed that only the rare-earth metal salts [Ce(NO₃)₃·6H₂O] and [Nd(NO₃)₃·6H₂O] showed moderate cytotoxicity against MCF-7 and HEC-1A cells, respectively.

CRediT author statement

Tatenda Madanhire: Writing- Original draft preparation, Investigation, Methodology

Hajierah Davids: Supervision, Writing- Reviewing and Editing

Melanie C. Pereira: Investigation

Eric C. Hosten: Investigation, Software, Validation

Abubak'r Abrahams: Supervision, Writing- Reviewing and Editing, Conceptualization

Declaration of interests

The authors declare that they have no known competing financial interests or personal relationships that could have appeared to influence the work reported in this paper.

The authors declare the following financial interests/personal relationships which may be considered as potential competing interests:

